Investigating the spatial distribution of the super-relaxed state of myosin in cardiac myofibrils using single-molecule microscopy

Ateeqa Naim

A thesis submitted to the University of Kent for the degree of Master of Science by Research in Biochemistry

September 2023

Supervisors: Professor Neil M. Kad and Professor Michael A. Geeves

Department of Biosciences

Declaration

Unless clearly stated and referenced otherwise, the work presented within this document is my own, carried out under the guidance of Professors Neil M. Kad and Michael A. Geeves within the Department of Biosciences at the University of Kent. The content of this document has not previously been submitted for examination at any other institution.

Acknowledgements

I would like to express my gratitude to my supervisor Prof. Neil Kad for his encouragement, guidance and support throughout this project. I also extend my sincere thanks to Prof. Micheal Geeves for his invaluable feedback and insights.

Further, I would like to thank all members of the Kad lab, collaborators, friends and family for their unwavering support and advice.

Abstract

Muscle contraction is a mechanism regulated primarily by the thick and thin filaments of the sarcomere, the smallest contractile unit of the muscle. Using single-molecule imaging we were able to investigate the ATP turnover rates of SRX myosin, a myosin state understood to be essential for maintaining contractile regulation. Our results revealed ATP turnover rates for the SRX state of myosin of ~ 0.006 s^{-1}, consistent with literature. We also developed a high-resolution imaging technique to spatially resolve ATP binding events, creating a map of myosin activity across the sarcomere. Our findings confirm the precision of these techniques and the potential for their use in providing a deeper understanding of contractile regulation within the cardiac myofibril. This work also provides the foundation for the comparison of ATP turnover rates and distribution of SRX myosin in cardiomyopathy mutated samples.

Table of Contents

Abbreviations

ADP	Adenosine Diphosphate
ATP	Adenosine Triphosphate
ATPase	Adenosine Triphosphatase
BDM	2,3-Butanedione Monoxime
C-zone	Central Zone
DRX	Disordered Relaxed
D-zone	Distal Zone
ELC	Essential Light Chain
F-actin	Fibrous Actin
HCM	Hypertrophic Cardiomyopathy
HMM	Heavy Meromyosin
LMM	Light Meromyosin
LV	Left Ventricle
MHC	Myosin Heavy Chains
MyBP-C	Myosin Binding Protein C
OAF	Oblique Angle Fluorescence
OD	Optical Density
PEP	Phosphoenolpyruvate
PK	Pyruvate Kinase
P-zone	Proximal Zone
RLC	Regulatory Light Chain
RT	Room Temperature

S1	Sub-Fragment 1
S2	Sub-Fragment 2
SNR	Singal-to-Noise Ratio
SRX	Super Relaxed
TIRF	Total Internal Reflection Fluorescence
Tm	Tropomyosin
Tn	Troponin
WT	Wildtype

1. Introduction

1.1 Human Muscle

Human muscles are categorised as skeletal, smooth and cardiac, each vital for the preservation of overall function and homeostasis of the body. Striated muscle: skeletal and cardiac, both share a striped appearance resulting from the sarcomere's highly organized assembly of actin and myosin filaments (Figure 1A & B). On the other hand, smooth muscle, located around visceral organs, has a uniform, non-striated appearance comprised of spindle-like fibres as seen in Figure 1C. This muscle group is distinguished by its ability to induce slow and steady contraction essential for the proper functioning of the digestive, respiratory, and reproductive systems (Brant B. Hafen and Bracken Burns, 2018).

Skeletal muscle is formed from long multinucleated fibres, has very prominent striations (Figure 1A) and is attached to the skeletal system, tongue, diaphragm, eye socket and upper oesophagus. These muscles are responsible for respiratory, locomotive, and postural functions (Frontera and Ochala, 2015; Heeransh D. Dave, Micah Shook and Matthew Varacallo, 2018).

Cardiac muscle, found exclusively in the heart, is characterised by its branched striated fibres connected by intercalated discs (Figure 1B) and is responsible for executing the heart's regulated and synchronised contractions (Rashelle Ripa *et al.*, 2023).

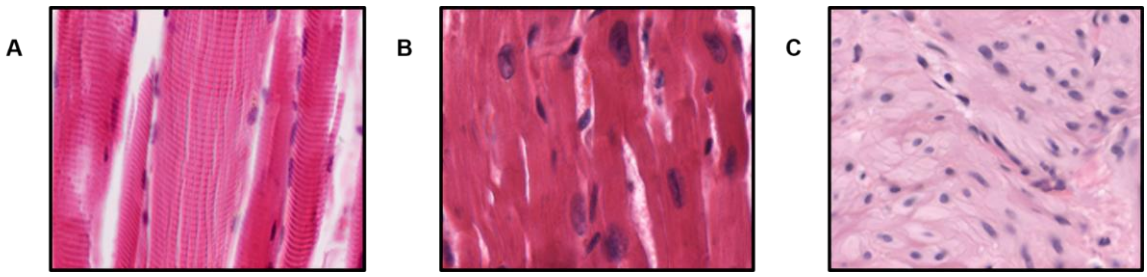

Figure 1. Histological Comparison of Muscle Structures. (A) Skeletal muscle and **(B)** Cardiac muscle share the same ultrastructure with their organised repeating sarcomeres resulting in their striated appearance. **(C)** Smooth muscle is made up of spindle-like cells providing the muscle with the uniform, non-striated structure.

1.2 The Sarcomere

The sarcomere is the fundamental contractile unit of striated muscle and is responsible for the conversion of energy released from hydrolysis of adenosine triphosphate (ATP) into mechanical work. The following sections explore the architecture of the sarcomere and the role each component contributes to the functioning of the whole cardiac contractile system.

The main two structural components of the sarcomere are the actin thin filament and the myosin thick filament, presented schematically in Figure 2. The actin thin filament (Figure 2A) is a double helical structure of coiled fibrous actin (F-actin) decorated with regulatory proteins: - tropomyosin (Tm) and troponin (Tn) (Yamada, Namba and Fujii, 2020). Figure 2B shows the thick filament, which is primarily comprised of myosin II, a hexameric protein, the coiled-coil tail region of which polymerizes to form the thick filament backbone. The globular head regions protrude out from the filament surface. The highly organised arrangement of these filaments creates the characteristic striated appearance of the sarcomere seen in Figure 3A (Tamborrini *et al.*, 2023).

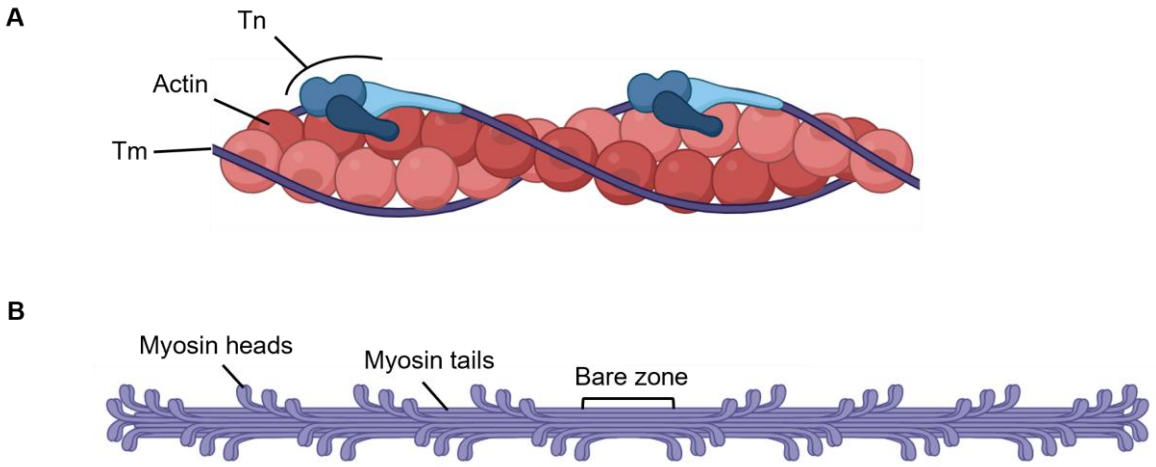

Figure 2. Schematic structure of sarcomere filaments. (A) Actin thin filament with regulatory proteins tropomyosin (Tm) and troponin (Tn). **(B)** Myosin thick filament with myosin heads, myosin tails and bare zone indicated. Produced in BioRender.

Each whole sarcomere is subdivided into lateral regions according to their ultrastructure (Figure 3): the I (isotropic)-band, located at either end of the sarcomere and populated only by the actin thin filament, the A (anisotropic)-band, housing both the thick and thin filaments and the H-zone in which only the thick filament and central M-line are present (Wang *et al.*, 2021). Delineating the lateral boundaries of each sarcomere are the Z-discs which are formed through antiparallel actin thin filaments of adjacent sarcomeres cross-linked by α-actinin molecules. Marking the centre of the sarcomere is the M-line, comprised of creatine kinase, myomesin and myomesin-2 (M-protein). The M-line anchors the thick filament through interactions between myomesin and myosin, preventing the filament from coming out of alignment during contraction (Lamber, Guicheney and Pinotsis, 2022). Another major component of the sarcomere is titin, the largest known protein, spanning the length of the half sarcomere with its N-terminus in the Z-disc and C-terminus in the M-line. Major roles of this protein include its function as a molecular spring, modulating the stiffness of the sarcomere. Within the thick filament, titin acts as an anchor for accessory proteins and provides stability to the filament's alignment in the sarcomere (Tonino *et al.*, 2017).

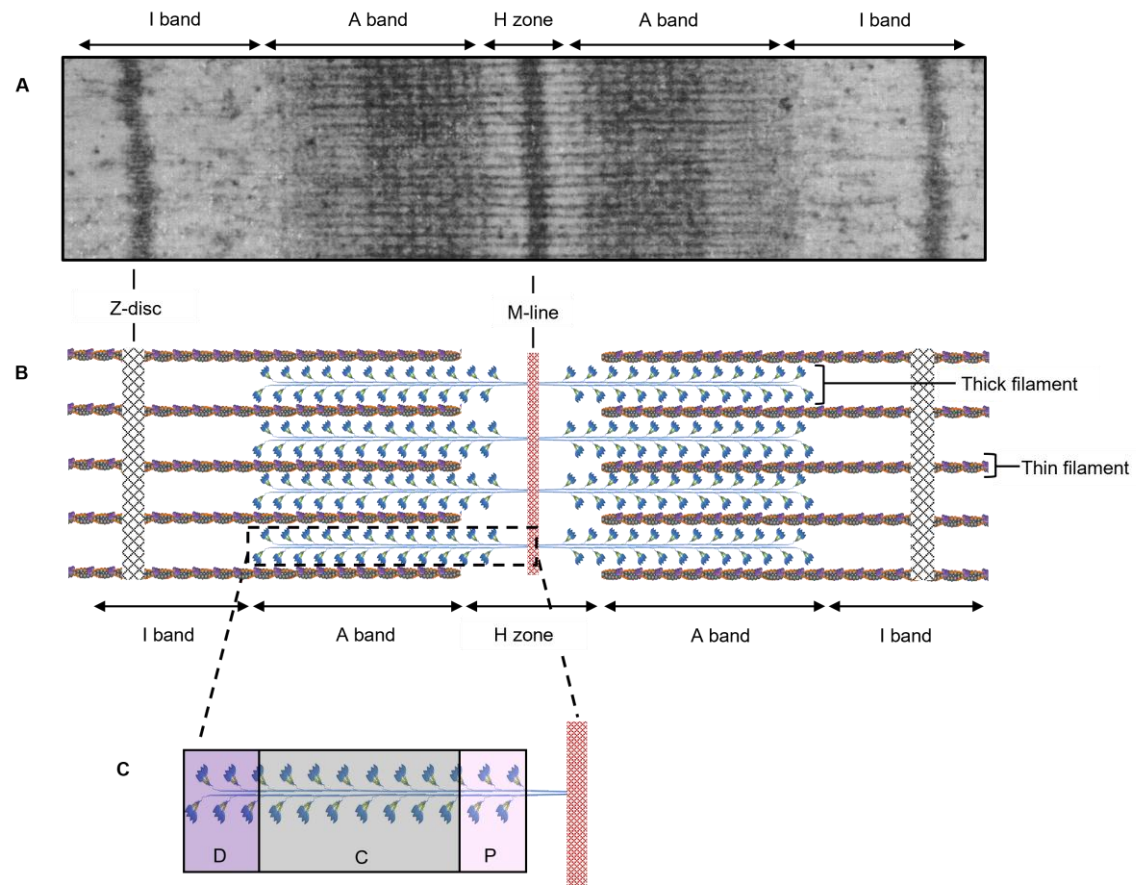

Figure 3. The structure of the sarcomere. (A) Electron micrograph of rabbit skeletal muscle adapted from Craig & Offer, 1976. **(B)** Schematic of the sarcomere with M-line, Z-disc, thick filament, and thin filament indicated. **(C)** Enlarged view of the thick filament indicated with P-, C- and D- zones indicated.

In each half sarcomere, the thick filament is divided into four regions: the proximal (P-), central (C-), distal (D-) and bare zones (Figure 3C). The bare zone and P-zone are in the H-zone of the sarcomere. The bare zone comprises antiparallel arrays of myosin tails with no heads extending onto the filament surface and marks the symmetry axis of the thick filament. The C-zone is the central region of the thick filament, characterized by the presence of the accessory protein myosin binding protein C (MyBP-C), arranged over nine stripes at ~430 Å intervals. The D-zone is the region of the filament most distal from the M-line (Huang *et al.*, 2023).

1.3 Structure of Myosin II

Muscle myosin (Myosin II) of the heart is the molecular motor protein responsible for powering cardiac contraction. As an adenosine triphosphatase (ATPase), myosin catalyses the hydrolysis of ATP into adenosine diphosphate (ADP) and inorganic phosphate (Pi). Hydrolysis of ATP releases energy, which is used by myosin II to generate pico-Newton forces for contraction when bound to the actin thin filament.

This force-generating powerhouse is comprised of two identical myosin heavy chains (MHCs) and two pairs of light chains; the essential light chain (ELC) and the regulatory light chain (RLC), shown in Figure 4 below.

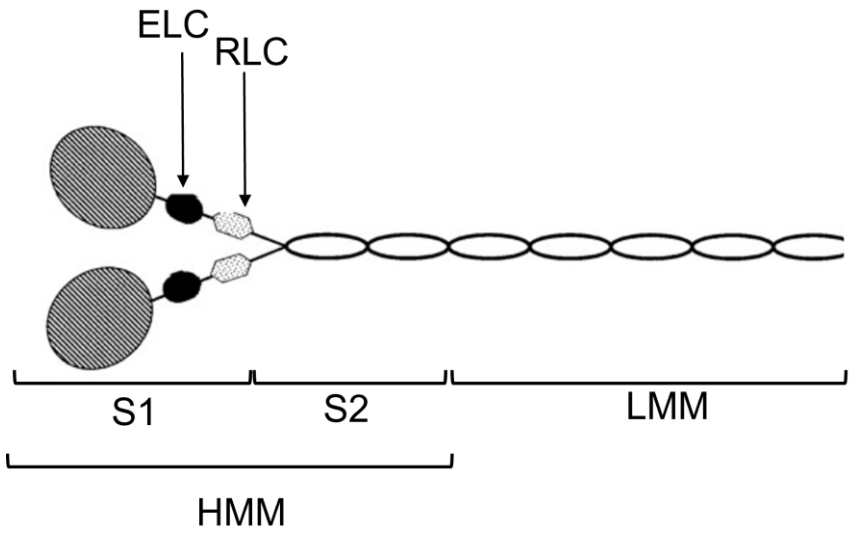

Figure 4 .The structure of Myosin II. Schematic of myosin II showing the sub-fragment 1 (S1), sub-fragment 2 (S2), essential light chain (ELC) and regulatory light chain (RLC) of the heavy meromyosin domain (HMM) and the light meromyosin domain (LMM). Figure adapted from Liu et al., 2016.

The MHCs are coiled-coil structures, with two proteolytic fragments: the heavy meromyosin (HMM) and the light meromyosin (LMM). The larger HMM yields two sub-fragments, sub-fragment 1 (S1) consisting of two globular head domains, with ATP and actin-binding sites, the lever arm, RLC and ELC. The two pairs of light chains regulate the movement of the globular

heads. Sub-fragment 2 (S2) is an α-helical coiled-coil domain linking the S1 to the LMM. The LMM is the coiled-coil rod region (tail) of the motor protein which attaches with the LMM of adjacent myosin to form the thick filament (Figure 2B) (Blair *et al.*, 2002; Suggs *et al.*, 2007; Miller *et al.*, 2009; Liu *et al.*, 2016).

1.4 Contraction

1.4.1 The Sliding Filament Theory and Cross Bridge Cycling

Simultaneously proposed by two independent groups, one led by Andrew F. Huxley and the other by Hugh E. Huxley in the 1950s, the sliding filament theory is a model that is quintessential for today's understanding of sarcomeric contraction. This model, presented schematically in Figure 5, describes the process of the actin thin filament sliding along the myosin thick filament towards the central M-line, resulting in the shortening of the sarcomere (Hanson and Huxley, 1953; Huxley and Niedergerke, 1954).

Additionally, Andrew F Huxley also proposed the cross-bridge cycle (Figure 5B), a theory describing the cyclic attachment and detachment of myosin heads with the actin thin filament producing the force necessary for the sliding of the filaments. Each cross-bridge is formed when a myosin head attaches to an available actin-binding site. In the absence of ATP, myosin and actin are strongly bound in a rigor complex. When present, ATP binds to the myosin head and is hydrolysed into ADP and P_i. P_i is released triggering the power stroke, where the bound myosin head bends forward pulling the thin filament towards the M-line. ADP is then released and the cycle repeats with a new ATP (Huxley, 1957).

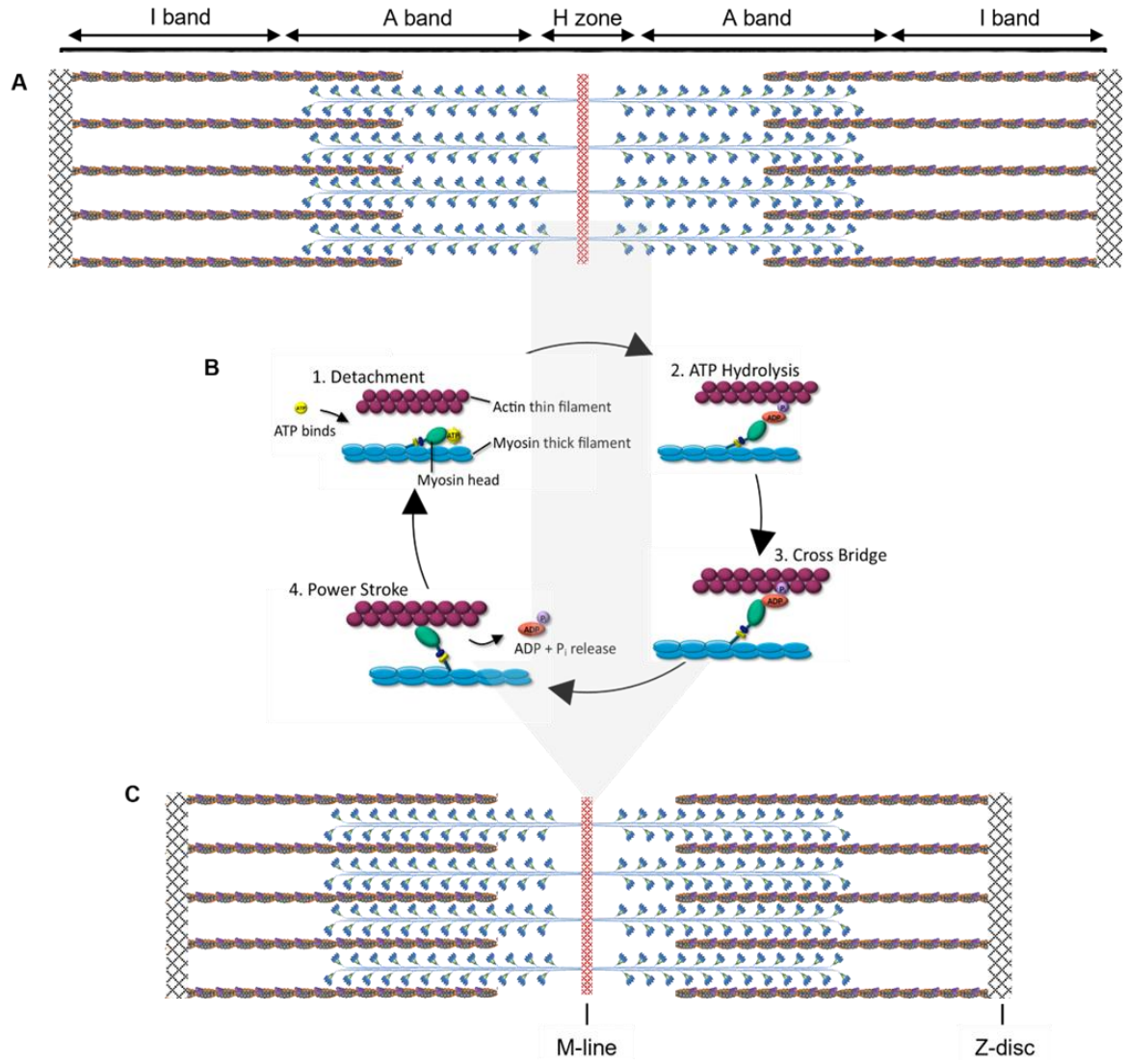

Figure 5. Sarcomere contraction. Schematic diagram of the sarcomere shortening during contraction as a result of the cross-bridge cycle and sliding filament model. **(A)** Relaxed sarcomere **(B)** Cross-bridge cycle **(C)** Contract sarcomere.

1.5 Contractile Regulation

Regulation of cardiac contractility is essential for the maintenance of overall cardiovascular function and health; therefore, several regulatory processes exist in the thin and thick filaments.

1.5.1 Contractile Regulation via The Thin Filament

Thin filament regulation is characterized by the modulation of access to actin binding sites via the regulatory proteins tropomyosin (Tm) and troponin (Tn) that decorate the thin filament, shown in Figure 6. Tm is a

double-stranded helical protein existing along the length of the actin filament blocking the actin-binding sites. Tn, a small globular protein, has three subunits: troponin C (Tn-C) which houses the calcium-binding sites, troponin I (Tn-I), inhibiting actomyosin binding when the muscle is in a relaxed state and troponin T (Tn-T) which binds Tn to Tm. This Tn complex collectively regulates the position of Tm. During an influx of intracellular calcium, calcium binds to Tn-C resulting in the conformational change shown in Figure 6, which, due to the binding of Tn to Tm, triggers Tm to move, exposing the actin-binding sites now available for actomyosin interactions (Yamada, Namba and Fujii, 2020).

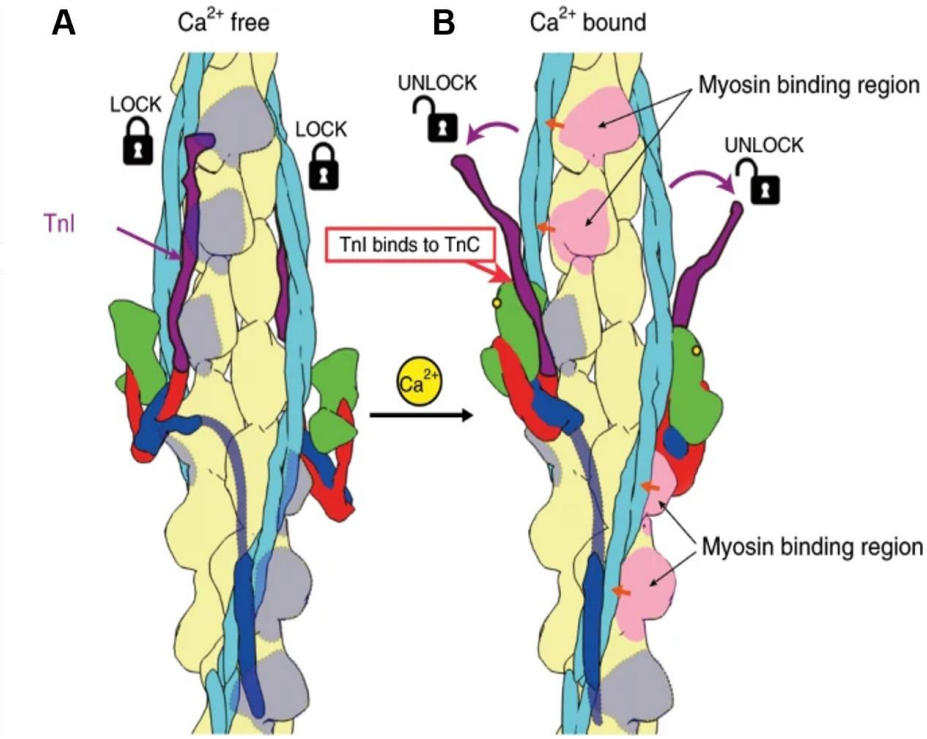

Figure 6. Thin filament regulation. Schematic displaying the freeing of blocked binding sites in the presence of calcium. In the calcium-free state **(A)** binding sites (grey) are blocked by Tm (light blue) which is anchored in place by the Tn complex (Green, dark blue and red). In the calcium-bound state **(B)** the Tn complex undergoes a conformational change releasing Tm which exposes the binding sites (pink). Adapted from Yamada, Namba and Fujii, 2020.

1.5.2 Contractile Regulation via The Thick Filament

The Super Relaxed State of Myosin

The calcium/thin filament mediated pathway described in section 1.5.1 is considered to provide the 'start' signal for contraction. On the other hand, the thick filament is understood to regulate contractile force and metabolic cost and governs adaptations to external load through systems that affect myosin and its availability to bind with the thin filament (Kampourakis, Sun and Irving, 2016).

For actomyosin binding, the head domain of myosin needs to be in close proximity to the thin filament, however, myosin can transition between three states: active, disordered relaxed (DRX) and super-relaxed (SRX), each of which have different affinities for actin as shown in Figure 7.

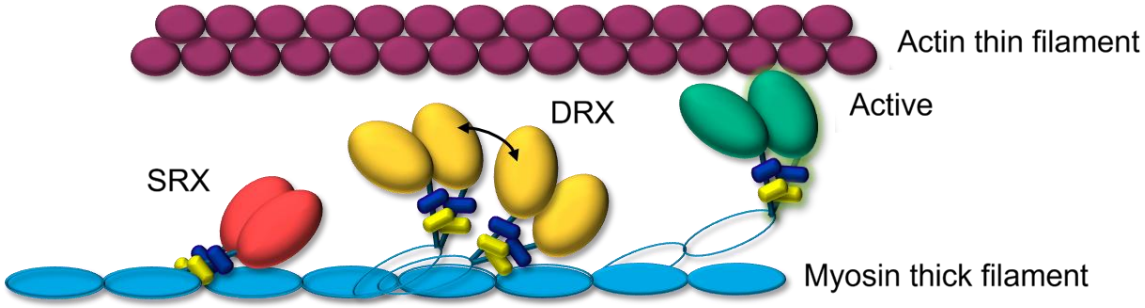

Figure 7. Comparison of the three myosin energy states. Active myosin (green) are those interacting with the thin filament. DRX myosin (yellow) are awaiting an available binding site and SRX myosin (red) are in a sequestered state, prevented from interacting with the thin filament.

When in the active state, the myosin is bound with actin and executes the power stroke (Figure 5B). Myosins in the DRX state are available for actin binding with the S1 regions existing in various conformations and proximities to the thin filament (hence 'disordered') and are waiting for binding sites to become available. Myosin in this state are measured to have an ATP turnover of ~ 0.05 s^{-1}. On the other hand, SRX myosins have an ATP

turnover rate up to ~10 times slower than DRX myosin. These myosins are suggested to interact with one another at their S1 regions and with the thick filament backbone. These interactions result in a sequestered state, preventing the myosin head from binding with actin, essentially rendering these myosins dormant and unable to contribute to muscle contraction (Hooijman, Stewart and Cooke, 2011; Heissler *et al.*, 2021; Walklate *et al.*, 2022).

Originally discovered in rabbit skeletal muscle, it was observed that SRX myosin were recruited into the DRX state upon muscle activation (Stewart *et al.*, 2010). However, in cardiac muscle this release upon muscle activation was not replicated (Hooijman, Stewart and Cooke, 2011). Instead, the proportion of SRX myosin in the relaxed vs active muscle remained constant. This sustained proportion of SRX myosin suggests the potential for a cardioprotective property of this state whereby a more ordered recruitment of myosin for force production is considered (Myburgh, Franks-Skiba and Cooke, 1995; Schmid and Toepfer, 2021)

Each active head acts as a force generator, with the total force produced by the sarcomere being the force generated by each head multiplied by the number of total force-generating (active) heads.

Equation 1.

$$F_{total} = F_{head} \times N$$

where F_{total} is the total force produced by the sarcomere, F_{head} is the force produced by one active head and N is the total number of active heads. Considering this and the functionality of cardiac muscle in comparison to skeletal, it is expected that these additional regulatory properties exist to

prevent force overload (Hooijman, Stewart and Cooke, 2011; McNamara, Singh and Sadayappan, 2019; Toepfer *et al.*, 2020; Nelson *et al.*, 2023).

Myosin Binding Protein C

Myosin binding protein C (MyBP-C) is a sarcomere accessory protein located at the thick filament and has three paralogs, slow skeletal (ssMyBP-C), fast skeletal (fsMyBp-C) and cardiac (cMyBP-C). Regardless of the paralog, MyBP-C exists only in the C zones of the thick filament in 7-9 regular stripes approximately 430 Å apart, resulting in a MyBP-C: myosin ratio of 1:3 (Heling, Geeves and Kad, 2020). This accessory protein is anchored to the thick filament via interactions with the LMM and titin (Tonino *et al.*, 2019). Although the mechanism by which cMyBP-C functions is not fully understood, it has been shown on multiple occasions to play an essential role in anchoring myosin in the SRX state and therefore an essential aspect of contractile regulation. (Stelzer, Fitzsimons and Moss, 2006; Kensler and Harris, 2008; Zoghbi *et al.*, 2008; McNamara *et al.*, 2016).

1.5 Contractile Dysregulation – Hypertrophic Cardiomyopathy

Hypertrophic cardiomyopathy (HCM) is an autosomal dominant disease with ~40% of causative mutations found in β-cardiac myosin (Adhikari et al., 2019). As seen in Figure 8, manifestation of HCM is asymmetrical, with the greatest hypertrophy occurring in the left ventricle's wall.

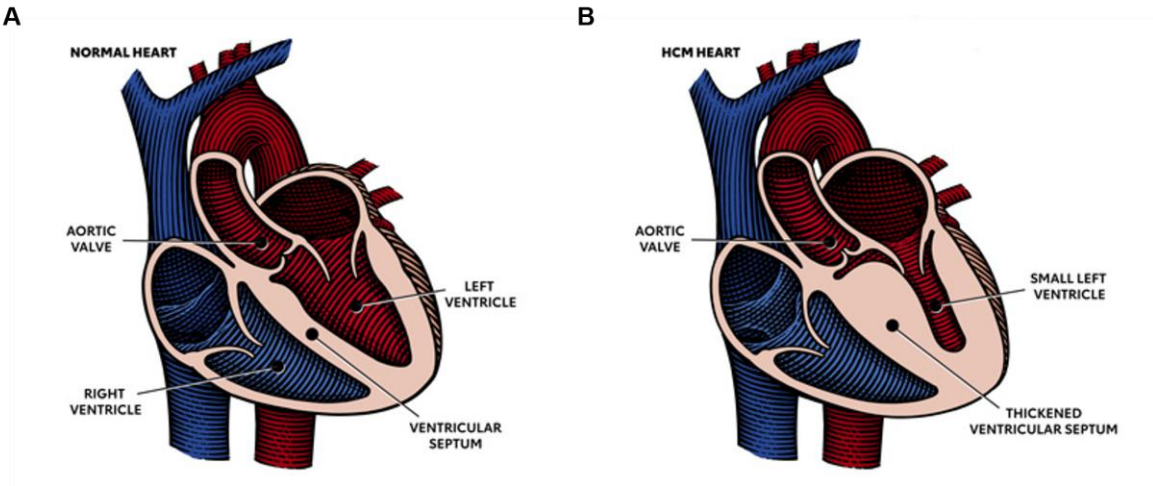

Figure 8. Comparison of normal and HCM heart. (A) Normal heart showing normal chamber capacities and no thickening of wall. HCM heart **(B)** showing extreme thickening of left ventricular walls and reduction in chamber size. Figure from American Heart Association, 2016.

Clinical symptoms of HCM include hypercontractility resulting from diastolic dysfunction yet preserved systole function. Given that increased force production results from an increase in force-generating heads (Equation 1.), it is assumed that HCM is the manifestation of dysregulation of the proportion of myosin in the SRX state (Woo *et al.*, 2003; Towbin, 2009; Vander Roest *et al.*, 2021).

1.6 Single-Molecule Imaging of ATP Turnover

1.6.1 Oblique Angle Fluorescence Microscopy

Standard imaging techniques such as epifluorescence and confocal microscopy are prevalent for their ability to provide comprehensive visualization of biological samples, with epifluorescence enabling rapid imaging of large areas and confocal offering enhanced resolution and optical sectioning of 3D structures (Fordham, Amos and White, 1987; Webb and Brown, 2012). However, as shown in Figure 9A and B, these techniques excite fluorophores through the entire sample depth resulting in a low signal-to-noise ratio (SNR) incompatible for single-molecule imaging. Total internal reflection fluorescence (TIRF) and Oblique angle fluorescence (OAF) microscopy are both single-molecule imaging techniques that provide high spatial resolution and SNR by altering the angle of illumination (Figure 9C & D). TIRF employs a critical angle of illumination to achieve total internal reflection at the interface of two media that have different refractive indices (a cover glass and immersion oil) to create an evanescent field that excites fluorophores. As the energy of the evanescent field decreases with distance from the media interface, only fluorophores near the coverslip are excited. OAF implements a similar approach to TIRF however uses a subcritical angle of illumination therefore allowing for excitation to penetrate deeper into the sample.

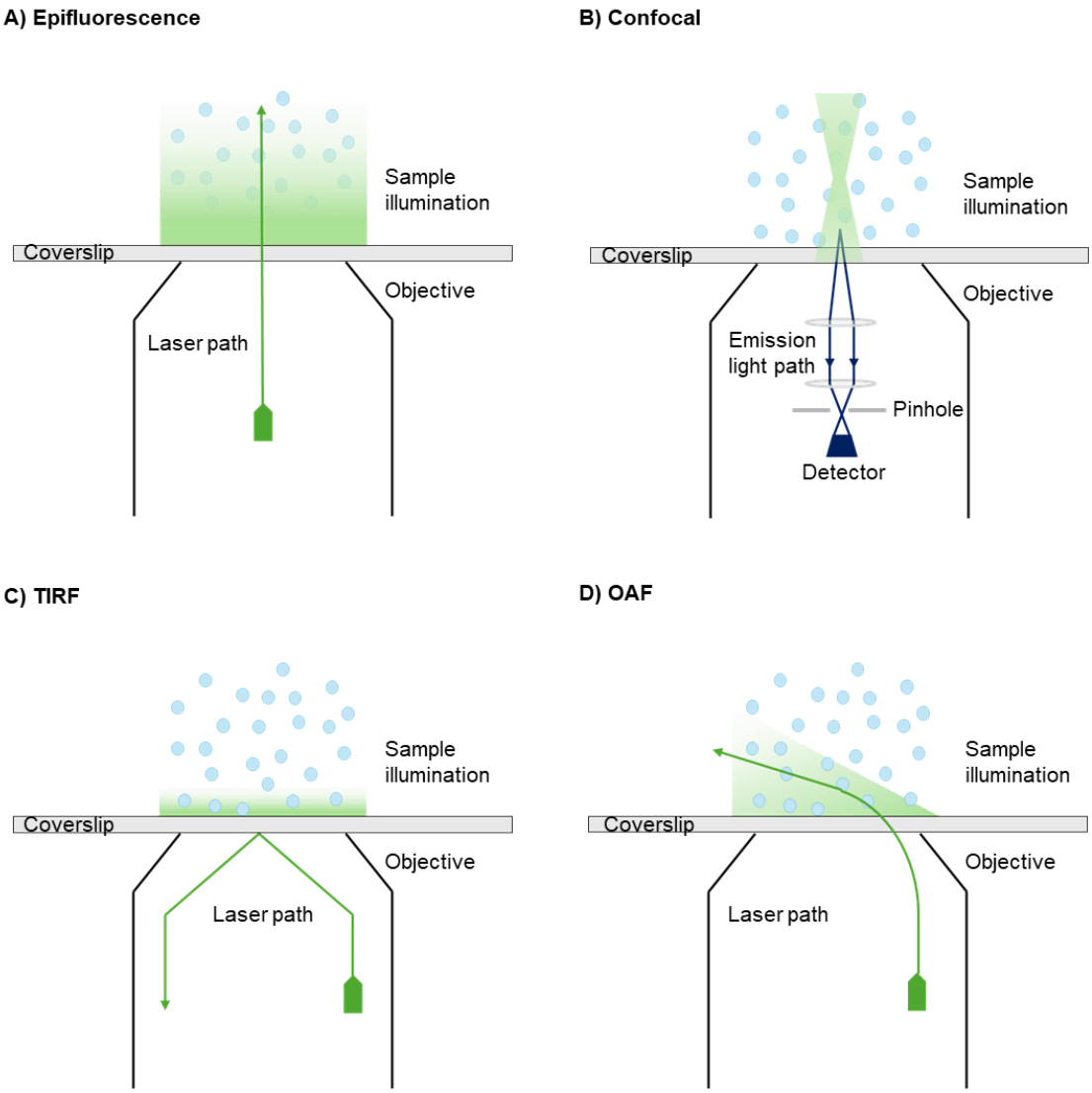

Figure 9. Illumination pathway used in microscopy techniques. A) Epifluorescence illuminates the entire sample depth by using a laser path that passes directly upwards through the sample. **B)** Confocal microscopy illuminates a specific point in the sample and then spatial pinholes are used to block out-of-focus emission light from entering the detector. **C)** Total Internal Reflection Fluorescence (TIRF) uses a critical angle to produce an evanescence illumination field to excite fluorophores ~0.2 -0.4 µm from the surface. **D)** Oblique Angle Fluorescence (OAF) uses an illumination beam at a subcritical angle to excite fluorophores deeper in the sample than TIRF.

With excitation confined to < 0.4 µm beyond the coverslip surface, TIRF is beneficial for imaging surface-bound interactions such as membrane protein dynamics. In contrast, OAF can penetrate up to ~5 µm into the sample

therefore offering more flexibility to image interactions occurring beyond the surface such as ATP binding (Desai, Geeves and Kad, 2015; Fish, 2022).

1.5.3 Cy3-ATP

The use of fluorescent probes enables the visualization of biomolecular processes with high spatial and temporal resolution. Cyanine 3 (Cy3) is a widely used photostable probe with excitation/emission peaks at 550 nm and 570 nm respectively. This probe can be conjugated with ATP to yield Cy3-edaATP (Cy3-ATP) without perturbing the nucleotide's biochemical properties, allowing for the direct visualization of ATP-dependent processes (Toseland and Webb, 2011).

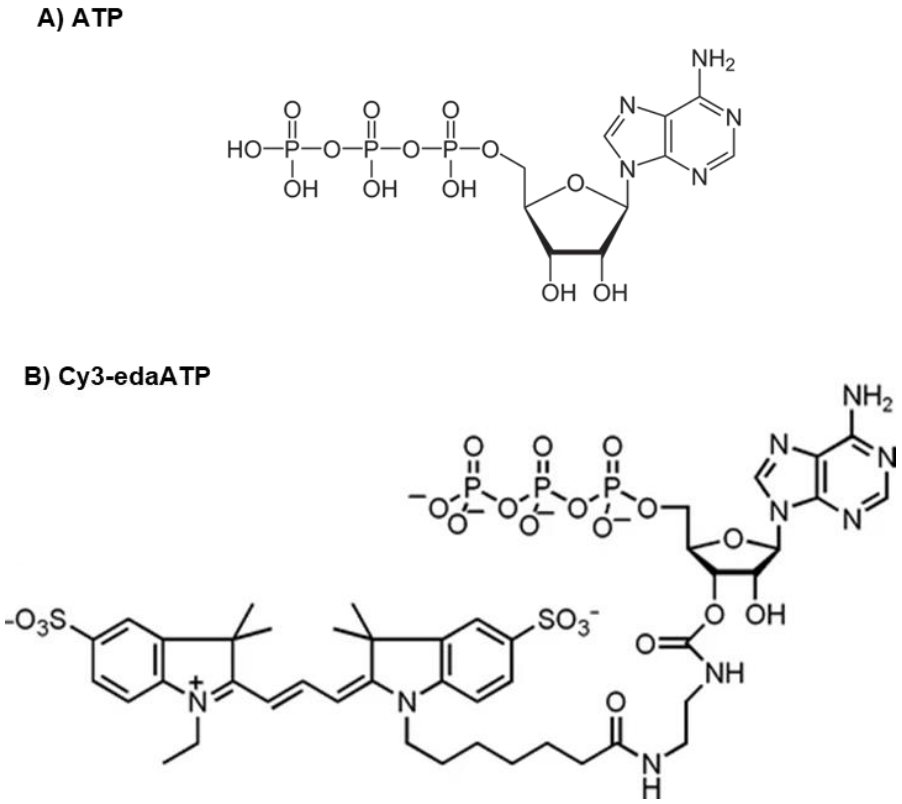

Figure 10. Chemical structure of ATP and the fluorescent analogue. A) ATP structure. **B)** Cy3-edaATP (Cy3-ATP). Figure adapted from Toseland and Webb, 2011.

Coupling the technique of OAF microscopy with the use of Cy3-ATP provides the ability to directly monitor the ATP consumption of myosins at a spatial resolution high enough that they can be mapped within the thick

filament zones. The photostability of the Cy3 also means that the entire binding events of the ATP can be imaged, therefore providing the ATP turnover time of each myosin and as a result, the energy state that the myosin is in.

Similar single-molecule imaging techniques have previously been used for the successful monitoring of the ATP turnover activities of myosin in striated muscle using BODIPY-ATP (Nelson *et al.*, 2020) and Cy3-ATP (Pilagov *et al.*, 2023). Both studies revealed exponentials representative of the DRX and SRX populations in relaxed muscle and were able to provide zonal distributions of these populations (Figure 11).

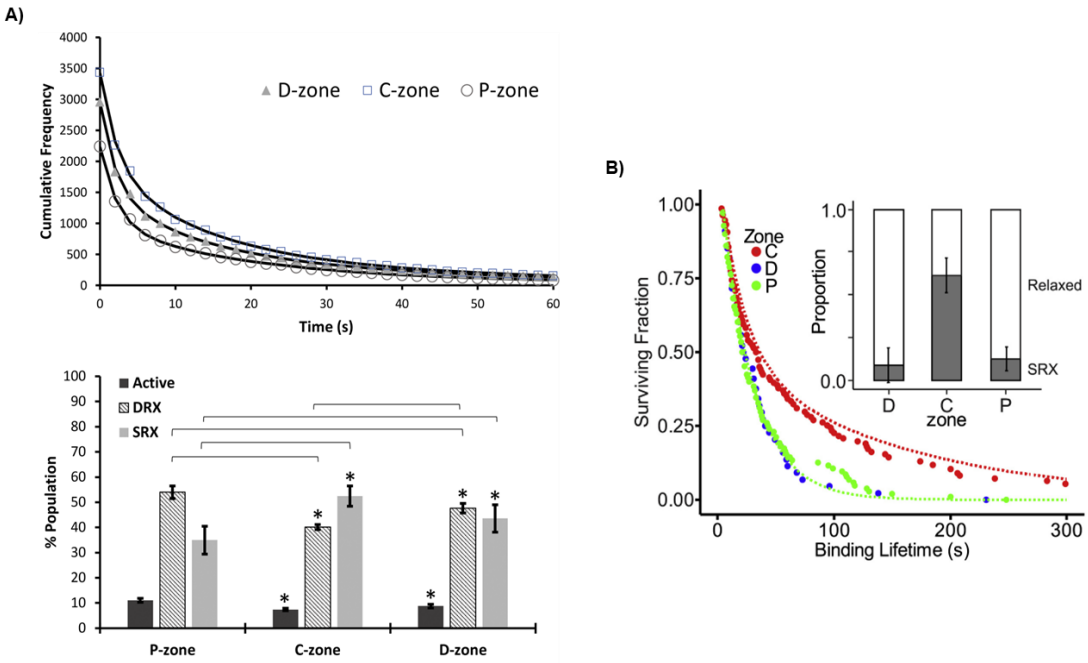

Figure 11. Spatial localization of fluorescent nucleotide binding events in relaxed skeletal muscle. Both studies show three survival decays localized to the P-, C- and D-zones of the thick filament. **A)** Survival decay of ATP binding events for each thick filament zone fitted to three exponentials. Histogram displays the % population breakdown for each myosin energy state in the thick filament zones. Adapted from Pilagov et al., 2023. **B)** Dashed lines represent theoretical curves if only DRX (green) or SRX (red) events were observed in the zone. Bar chart shows the proportions of SRX (grey) and DRX (white) events. Error bars are standard errors for exponential fits. Adapted from Nelson et al., 2020.

1.7 Aims of this Thesis

Myosin II transitions between three energetic states; Active, DRX and SRX, characterised by different ATP hydrolysis rates. Active myosins, occurring in active muscle in the presence of calcium, have a rapid ATP turnover of < 10 seconds (~0.8 s^{-1}). Myosin in the DRX state are present in active and relaxed muscle and hydrolyse ATP at ~0.05 s^{-1}. SRX myosins have a significantly reduced rate of ~0.005 s^{-1}. In healthy cardiac muscle, the SRX population is preserved in relaxed and active conditions, acting as a reserve pool and recruited only under extreme stress. However, ablation or dysregulation of this SRX population may be the cause of cardiomyopathies such as HCM.

This project aims to optimise the imaging of ATP consumption in relaxed cardiac muscle, allowing for the measurement of ATP turnover rates and determination of the zonal distribution of the DRX and SRX populations. Furthermore, this project will also focus on developing a novel high-resolution imaging technique to facilitate the mapping of myosin activity across the thick filament at a <50 nm spatial resolution. This technique will allow for understanding the regulation of myosin activity and recruitment into the higher/lower energy states in more spatial detail than just at the level of the thick filament zones. It will also help to determine if/how myosins cooperatively interact to recruit neighbouring myosins and where precisely these interactions occur along the filament. These techniques can then be employed to understand the role, if any, that sarcomere accessory proteins contribute to regulating myosin recruitment and the implications that mutations have on this regulation.

2. Materials and Methods

2.1 Buffers

Cardioplegic solution: 5.5 mM Glucose, 0.5 mM $MgSO_4$, 24 mM KCl, 20 mM $NaHCO_3$, 109 mM NaCl, 0.9 mM H_2NaO_4P, 1.8 mM $CaCl_2$, 0.01% NaN_3, pH 7.4.

Permeabilization buffer: 20 mM MOPS, 132 mM NaCl, 5 mM KCl, 4 mM $MgCl_2$, 5 mM EGTA, 10 mM NaN_3, 5 mM DTT, 20 mM BDM, EGTA-free Protease inhibitor cocktail (A32965; Thermo Scientific), 0.5% Triton X-100, pH 7.1 at room temperature (RT)

BDM buffer: 20 mM MOPS, 132 mM NaCl, 5 mM KCl, 4 mM $MgCl_2$, 5 mM EGTA, 10 mM NaN_3, 5 mM DTT, 20 mM BDM, EGTA-free Protease inhibitor cocktail (A32965; Thermo Scientific), pH 7.1 at RT

No BDM buffer: 20 mM MOPS, 132 mM NaCl, 5 mM KCl, 4 mM $MgCl_2$, 5 mM EGTA, 10 mM NaN_3, 5 mM DTT, EGTA-free Protease cocktail (A32965; Thermo Scientific), pH 7.1 at RT

Imaging buffer: 20 mM MOPS, 132 mM NaCl, 5 mM KCl, 4 mM $MgCl_2$, 5 mM EGTA, 10 mM NaN_3, 5 mM DTT, 3.25 mM ATP, 3 nM Cy3-ATP, 2 mM Trolox. pH 7.1 at RT.

Cy3-ATP was synthesized and kindly provided by Dr C.P. Toseland (University of Sheffield, Sheffield, UK)(Toseland and Webb, 2011)

Myofibrils used in this study were porcine cardiac left ventricle trabeculae and were isolated on-site using the following procedures.

2.2 Imaging Chamber Construction

All single-molecule experiments were carried out using imaging flow chambers (Figure 12). For the base of the structure, a standard microscope slide with two 3 mm holes, drilled in the centre 15 mm apart, for the in- and outflow of sample, was used. Borosilicate coverslips (Menzel Gläser, 24 x 40 mm, 1.5 thickness) and drilled slides were soaked in 100 % ethanol overnight then plasma cleaned (Plasma cleaner PDC-32G-2, Harrick Plasma) to ensure surfaces were free of organic contaminants and to increase hydrophilic properties. Following this, 15 µg/ml Poly-L-Lysine (PLL) was spread across the surface of a plasma-cleaned coverslip and left to dry for 30 minutes. To assemble the flow chamber, a 10 mm x 20 mm x 0.18 mm gasket was cut from double-sided tape using a Cricut Explore Air 2 and sandwiched between the drilled slide and PLL-coated coverslip (Figure 12). The assembled chamber had a capacity of ~30 µl.

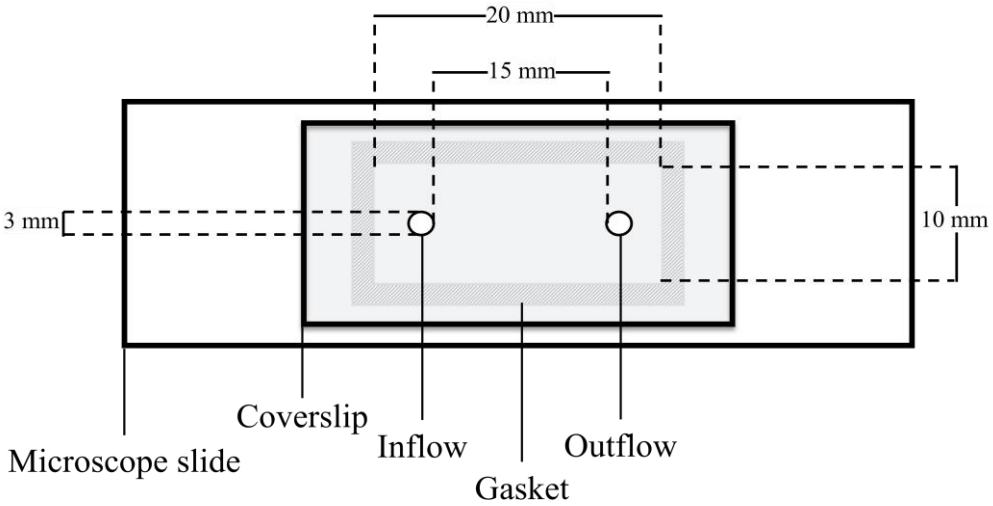

Figure 12. Imaging flow chamber. Plasma-cleaned and PLL-coated borosilicate coverslip (24 x 40 mm) is adhered to a plasma-cleaned microscope slide (with in- and outflow holes) using a 180 µm thick gasket resulting in an imaging chamber with a fluid capacity of 30 µl. Figure is not to scale.

2.3 Dissection and Storage of Porcine Heart

Immediately following excision, the heart of a freshly euthanized adult farm pig was submerged in ice-cold cardioplegic solution.

Whilst in solution, left ventricular (LV) trabeculae samples were extracted from the heart and cut down into pieces of approx. 5 mm diameter and no thicker than approx. 3 mm, flash frozen and kept at -80 °C for long-term storage.

2.4 Sample Preparation and Image Acquisition for Imaging ATP Turnover

2.4.1 Permeabilization of Porcine Cardiac Tissue

A single LV sample was rapidly thawed in permeabilization buffer on ice and cut into approximately 2-3 mm thick strips, following the direction of muscle fibres using 9 mm Vannas scissors (Duckworth & Kent). The strips were secured to a silicon-based plate with tungsten rods at either end to prevent them from moving across the plate and to apply slight tension, aiding the penetration of Triton X-100. These were left overnight at 4 °C on a rotary shaker. After permeabilization, samples were rinsed with BDM buffer three times to remove Triton X-100.

2.4.2 Homogenization of Permeabilized Tissue

For myofibril isolation, the rinsed permeabilized tissue was cut into 1 mm thick strips and transferred to a 2 ml microcentrifuge tube with 500 µl BDM buffer. The samples were then homogenized using a Tissue Ruptor II at medium-low speed for 10 seconds twice, with a 1-minute break on ice in between. The homogenizer probe was first primed with 500 µl BDM buffer alone to prevent myofibrils from sticking.

2.4.3 Fluorescent Labelling of Isolated Myofibrils

To prepare myofibrils for imaging, the Z-discs of the sarcomere were fluorescently labelled with 5.5 nM Alexa488 Goat anti-Mouse IgG (conjugated with 11 nM Monoclonal anti-α-actinin) in 30 µl of myofibril suspension for 1.5 hours, at 4 °C on a rotator with 1 mg/ml BSA.

To maintain a consistent myofibril/antibody ratio across sample preparations, the optical density (OD) of myofibril suspensions were maintained in a range of OD_{600} 0.39 – 0.42 by either diluting or concentrating the suspension (prior to fluorescent labelling) where necessary, with either the addition of BDM buffer or by allowing myofibrils to settle then removing the necessary volume of BDM buffer from the surface.

2.4.4 Preparation of Imaging Chamber with Labelled Myofibrils for Imaging

For imaging, labelled myofibrils were injected into the previously assembled imaging chamber (Section 2.2). 100 µl BDM buffer followed by the tagged myofibril suspension was flushed into the assembled microfluidic imaging chamber. Filling the chamber with the BDM buffer before the myofibril suspension facilitated the diffusion of myofibrils across the chamber, rather than them collecting at the entrance (Laurens Heling, 2019). The chamber was incubated coverslip side down at 4 °C for 30 minutes to allow myofibrils to adhere to the coverslip surface.

Excess non-adherent myofibrils and BDM were flushed out of the chamber with two washes of 100 µl No BDM buffer, with a 1-minute break at 4 °C in between washes. Finally, 100 µl of Imaging buffer was flushed

into the chamber and the drilled holes were sealed with tape to minimize airflow through the chamber.

All solutions were flushed into the chamber at a flow rate of ~100 µl/min to ensure myofibrils were not dislodged from the surface.

2.4.5 Image Acquisition

All single molecule data was collected using a custom Oblique Angle Fluorescent (OAF) microscope detailed in Desai et al., 2015. Briefly, the system, built into an Olympus IX50 frame, contains a long focal length anti-reflection coated plano-convex lens (250 mm, Thorlabs) which focuses the incident laser beam onto the back focal plane of an Olympus PlanApo 100x 1.45 numerical aperture objective lens. The resulting collimated beam is translated using a gimbal-mounted mirror (Thorlabs) to produce an obliquely angled beam (Desai, Geeves and Kad, 2015). This results in a subcritical angle of illumination which limits background illumination resulting in an increased SNR (Section 1.6.1, Figure 9 D).

For excitation of Cy3, a 561 nm diode OBIS LS laser (Coherent, USA) was used at 20 mW and a 488 nm diode Oxxius laser at 18 mW was used for excitation of Alexa488. Lasers were controlled via Coherent connection and Oxxius micromanager respectively.

To locate myofibrils, a brightfield camera (Swann, C500 CCD Colour Camera) was used to prevent photobleaching of the sample. The system was then switched to the Orca Flash 4.2 camera (Hamamatsu, pixel size 6.5 µm equivalent to 63.2 nm for the image) and the lasers were switched on for data collection.

Data was collected as 1000-frame videos, with every six-frame repeat being made up of five Cy3-ATP frames and one Z disc frame (Figure 13). The images were taken through a central channel in which the emissions of both fluorophores could be detected. This frame sequence was essential as having the frequent Z-disc frames in between the Cy3-ATP frames allowed for accurate tracking and correction of any myofibril drift detailed later in section 2.6.2.

To maintain this frame sequence and to extend the lifetime of the fluorophores before they were photobleached, stroboscopic illumination of the sample was used. The lasers and camera were connected to an Arduino board allowing for a custom-written Arduino script to be used to control them. With this script, the 561 nm laser and camera were switched on to capture one frame of the Cy3-ATP. The laser and camera were then switched off for 2 seconds before the script looped back to take a total of five Cy3-ATP frames before moving onto the one Z-disc frame. The script followed the same procedure for the Z-disc frame except now, the 488 nm laser was turned on and only one frame was taken before looping back to take the next series of frames. Figure 13 provides a simplified flowchart to illustrate the imaging sequence described here.

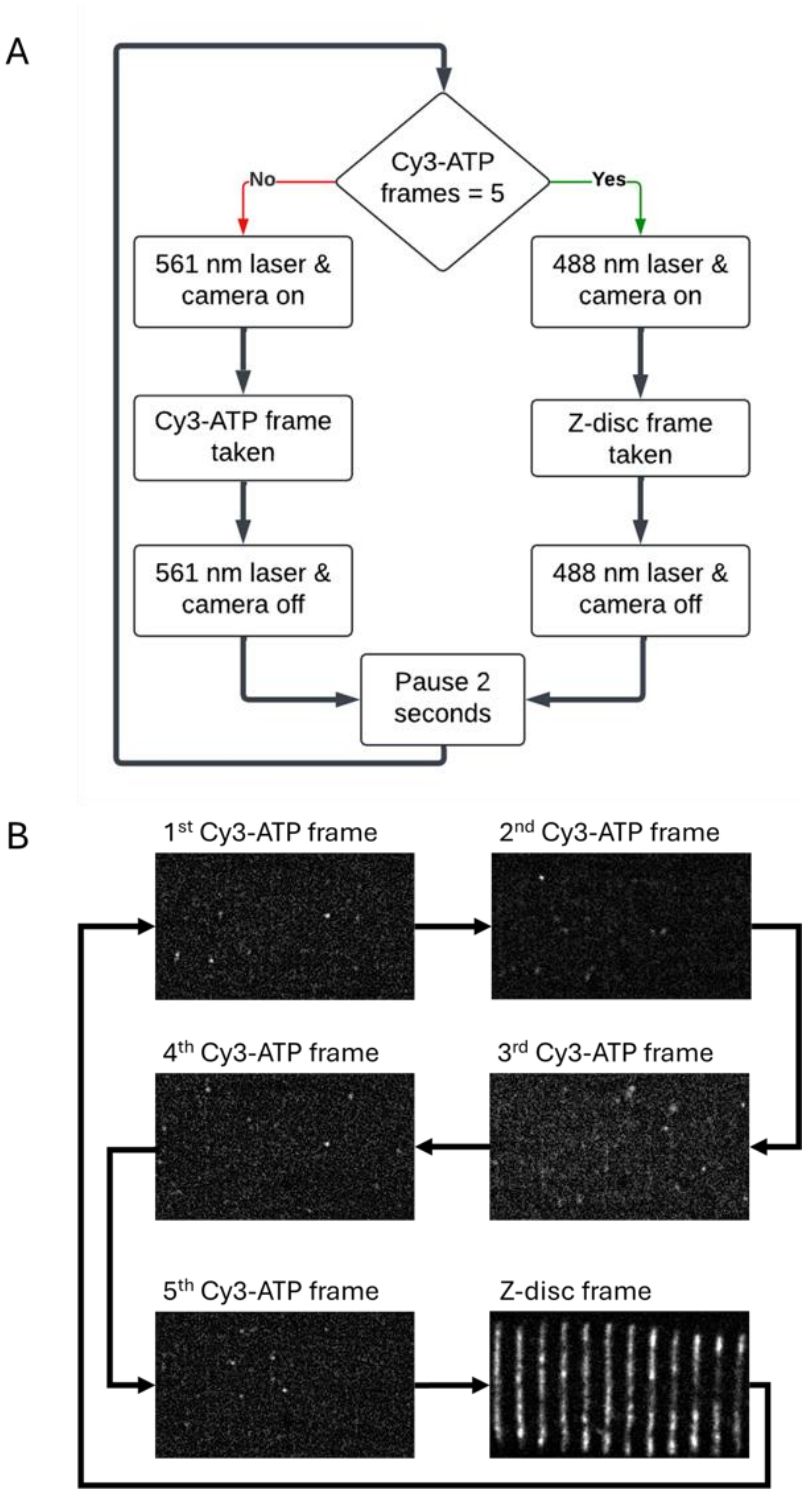

Figure 13. Simplified flowchart to illustrate the imaging sequence used for collection of ATP turnover data. (A) Flow chart showing a simplified overview of the Arduino script used to control the 488 nm diode Oxxius laser, the 561 nm diode OBIS LS laser and the Orca Flash 4.2 camera to maintain the frame sequence**. (B)** Example of one frame sequence taken of a porcine cardiac LV myofibril with five Cy3-ATP frames and one Z disc frame. Contrast of images were increased for ease of viewing.

2.5 Sample Preparation and Image Acquisition for High-Resolution Imaging of the Spatial Distribution of Myosin Activity

Sample preparation for the high-resolution imaging approach is similar to that used for the imaging of the ATP turnover rates (Section 2.4). However, a few alterations were introduced at this stage to facilitate faster sample preparation i.e., eliminating the need to permeabilize the sample overnight. These modifications were adapted from Nelson et al., 2023.

Briefly, frozen porcine LV samples were rapidly thawed in BDM buffer and cut down to strips of approximately 1 mm thickness. Tissue strips were homogenized as described in section 2.4.2. For permeabilization, tissue was collected by centrifugation at 1000 RCF for 4 minutes at 4 °C, then resuspended and permeabilized in 1% Triton X-100 permeabilisation buffer for 30 minutes at 4 °C, rotating. Permeabilized tissue was collected by centrifugation at 1000 RCF for 4 minutes at 4 °C and washed with BDM buffer 3 times to remove Triton X-100. Isolated myofibrils were fluorescently labelled and prepared for imaging in imaging chambers as described in section 2.4.3 and section 2.4.4.

2.5.2 High-Resolution Imaging

As stated, all single molecule data was collected using a custom OAF microscope (Section 2.4.5). This imaging approach was largely similar to that described in section 2.4.5 however some alterations were introduced so Cy3-ATP could be photobleached in between each frame.

The power for the 561 nm diode OBIS LS laser (Coherent, USA) was increased from 20 mW to 40 mW (as indicated in the Oxxius micromanager software) and was set to continuously emit rather than stroboscopically.

Additionally, the frame gap between each Cy3-ATP frame was increased from 2 seconds to 5 seconds and the imaging period remained at 30 minutes, resulting in the total number of frames collected per video to be halved to 500, compared to the 1000 frames used for collecting ATP turnover rates.

2.6 Data Analysis

2.6.1 Single-molecule tracking

Due to the oblique angle of illumination used; the excitation light only excites fluorophores that are within the myofibril rather than also exciting those that are around the outside (Section 1.6.1). Additionally, the absence of movement of Cy3-ATP molecules during the 200 ms frame capture indicates their binding to myosin, as any unbound molecules would appear blurred. Therefore, we can assume that all observed Cy3-ATP fluorescence is of those molecules that are bound with a myosin. From hereafter Cy3-ATP fluorescence observed within a myofibril will be referred to as an ATP binding event.

To extract the spatiotemporal data of each ATP binding event and the Z-disc positions, the ImageJ plugin Trackmate was used as it provides an unbiased automated approach to detect spots from images and track them over time (Schindelin *et al.*, 2012; Tinevez *et al.*, 2017). To prevent spurious objects from being tracked, the minimum intensity threshold for the tracks was manually adjusted. This intensity threshold was amended on a sample-to-sample basis as this was affected by the SNR of each video. Parameters that remained constant were the linking distance, gap max closing distance, max frame gap and the estimated object diameter for the Laplacian of Gaussian (LoG) detection (set to 360 nm). The linking distance (set to 100 nm) is the maximum distance a single track could have shifted in the

subsequent frame before being recorded as two separate events. The gap max closing distance (set to 100 nm) works in conjunction with the max frame gap (set to 5 frames). With these two parameters, if a Cy3-ATP binding event appeared within 100 nm of another binding event less than 6 frames before, these would have been recorded as a single event.

The x and y coordinates and duration of each track from all frames were extracted into a Microsoft Excel file and plotted to show the Z-disc and ATP binding event positions (Figure 14).

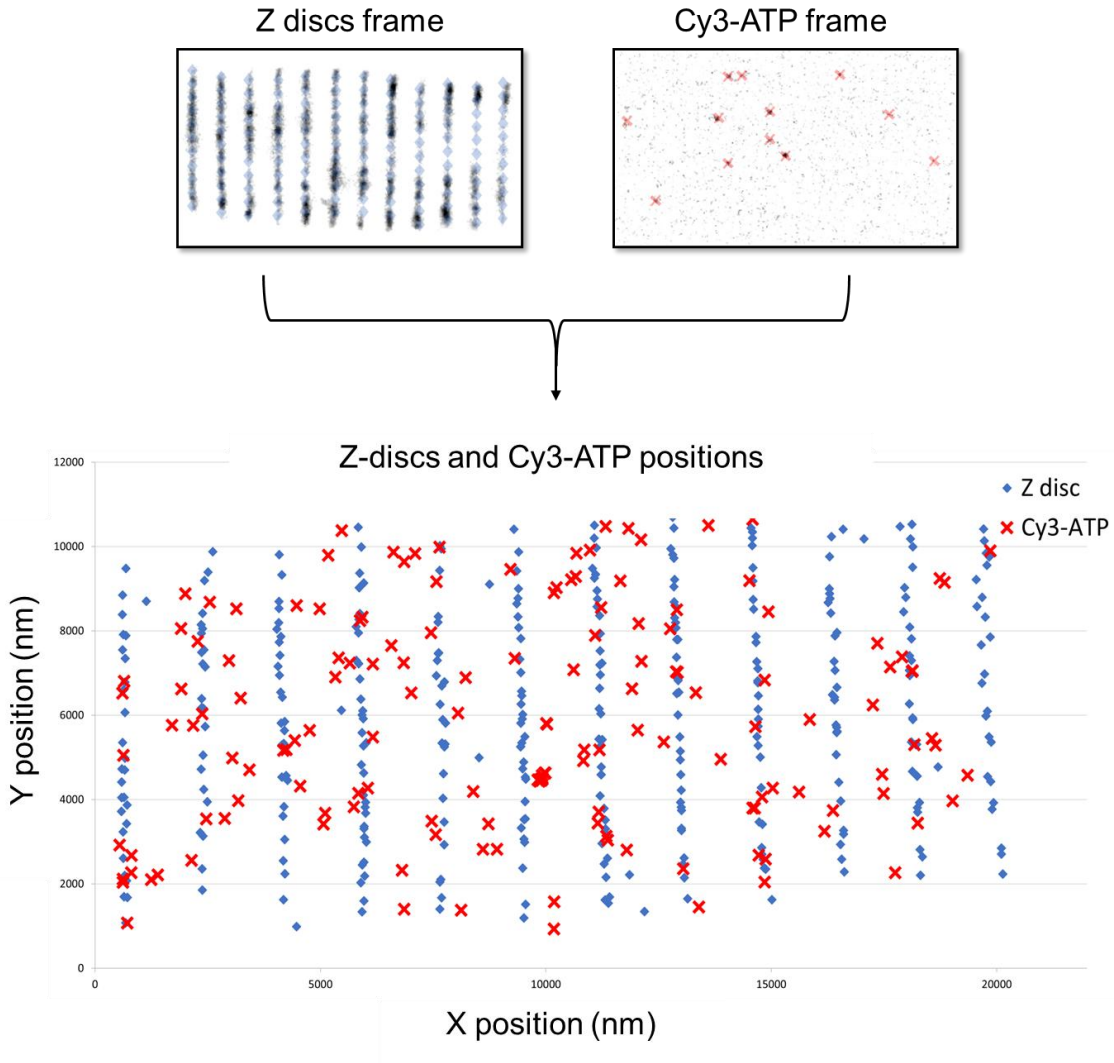

Figure 14. Z-disc and ATP binding event positions extracted using Trackmate. Blue diamonds represent the track spots for the Z-disc positions and red crosses are ATP-binding event tracks. Spot positions are extracted using Trackmate, preventing bias and errors. Figures for Z-disc and Cy3-ATP frames are inverted for ease of viewing.

2.6.2 Drift Correction

Samples would occasionally drift through x and/or y planes over the course of the imaging period. Correction of erroneous sample movement was performed using a drift correction ImageJ plugin (mpicbg-scicomp, 2017). This plugin works by calculating the drift of user-selected landmarks that are present throughout the entire video, in this case, the Z-disc positions were used. The plugin then shifts successive frames using linear interpolation to calculate the required shift. Drift correction is performed prior to Trackmate, where necessary.

2.6.3 Tilt Correction

For ATP binding positions to be localized relative to the sarcomere their x positions had to be related to those of the Z-discs. However, on occasion, the Z discs would not be perpendicular to the axis and to extract accurate event positions this tilt had to be corrected (Figure 15). To do this, the x coordinates of the left- and rightmost tracks of the Z-disc were used as minimum and maximum parameters for a search of all Z-disc tracks that lay within these points. All positional data for this sarcomere were then corrected by calculating the rotation of each point about the left-most Z-disc track using the slope of the tilted Z-disc to determine the angle of rotation. This adjustment was carried out in Microsoft Excel for each sarcomere individually.

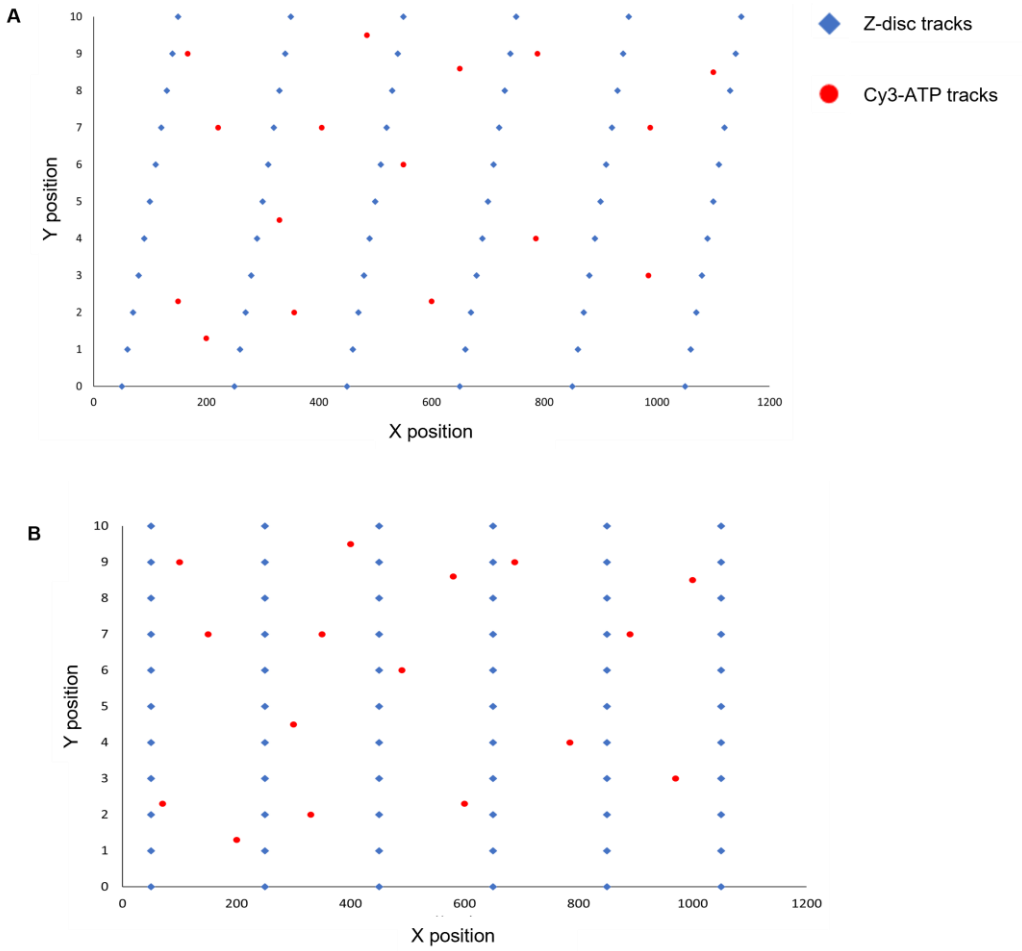

Figure 15. Tilt correction of sarcomere Z-disc and ATP binding event positions. (A) Z-discs and ATP binding event positions prior to tilt correction. **(B)** Positions of Z-discs and ATP binding positions after tilt correction. Tilt is corrected and the binding event positions in relation to the Z-discs not altered. Figures are a representation and not actual data.

2.6.4 Sub-sarcomeric Zone Boundaries & Zoning the Cy3-ATP binding events.

Assigning sub-sarcomeric zone boundaries was a crucial step in localizing Cy3-ATP events to zones. The central M-line was determined for each sarcomere by binning the coordinates of the tilt-corrected tracks of the left and right Z-disc of the sarcomere and then fitting these bins to a Gaussian distribution. The accuracy of this user-free determination of the sarcomere centres is 31.8 nm, calculated from the average SD of 1,318 Z-disc Gaussian

fits. With the midpoint of the sarcomeres, the coordinates for each sub-sarcomeric zone boundary were also determined.

Cy3-ATP binding event x coordinates were cross-referenced with those of the sub-sarcomeric zones for the spatial distribution of events.

2.6.5 Kinetics

The following analysis is only applied to the data for the investigation of myosin ATP turnover rates.

In addition to the location, we recorded the time that each ATP binding event was visible for. This lifetime indicates how long the myosin took to turnover this molecule of ATP because once released, the molecule leaves the myofibril (i.e., the excitation field). These lifetimes of each binding event were binned at the frame interval (2 seconds), i.e., binning all events with lifetimes within 2 seconds of one another together. These binned lifetimes were fit to three exponentials, fittings to more exponentials were also tested however three exponentials provided the best fit, determined by examination of the residuals. Rates were calculated according to

Equation 2.

$$A_t = A_0 \cdot e^{(-k \cdot t)}$$

where A_t is the amplitude of Cy3-ATP tracks at time t, A_0 is the amplitude of Cy3-ATP tracks at time 0s, e is the exponential and k is the rate. The survival frequency was fit to the sum of the three exponentials, providing a triple exponential fit. However, repeated data in the survival frequency were excluded to prevent overweighting of fits. Furthermore, the Microsoft Excel tool 'Solver' was used for the fitting, to reduce user interference, correcting the fit for the minimum SSD or SSDln.

3. Investigating β-cardiac Myosin's ATP turnover in Porcine Myofibrils

3.1 Introduction

The primary task for this project was the optimization of this single-molecule imaging technique for use with cardiac myofibril samples. The following section describes the optimizations that the baseline protocol, which was originally developed for skeletal myofibrils and described in Pilagov et al., 2023 underwent.

With successful optimizations of the protocol, it was possible to move forward with collecting the ATP turnover data for WT porcine cardiac left ventricle (LV) myofibrils. The LV was selected for use in these experiments as β-cardiac myosin is the dominant isoform present. This isoform is where 40% of all HCM-causing mutations occur (Adhikari *et al.*, 2019).

3.2 Results

3.2.1 Improving the Quality of Myofibrils for Single Molecule Imaging

Initially, an already optimized skeletal myofibril preparation protocol (Pilagov *et al.*, 2023) was used for cardiac muscle as this provided a starting point from which optimizations could be carried out.

Inadequate fluorescent staining of the Z-discs and myofibril fragments that were too small were the initial issues that required optimizations. Z-discs act as the fiducial markers for ATP binding events, therefore poor staining results in an inability to accurately localize ATP binding events to sub-sarcomeric regions.

Initially, fluorescent staining of Z-discs was carried out after the myofibrils had been introduced to the imaging chamber. This approach led to a reduced antibody binding susceptibility in areas of myofibrils that were in contact with the cover glass, resulting in these regions having lower fluorescence intensity (Figure 16A). To overcome this, the labelling was performed in solution prior to the myofibrils being injected into the chamber, with no changes made to the antibody concentration or the OD_{600} of myofibril suspension. This resulted in more fluorophores being able to attach to the Z-discs, therefore a more even labelling across the myofibril and a higher fluorescent intensity. Figure 16 compares the labelling of porcine cardiac LV myofibrils under both conditions.

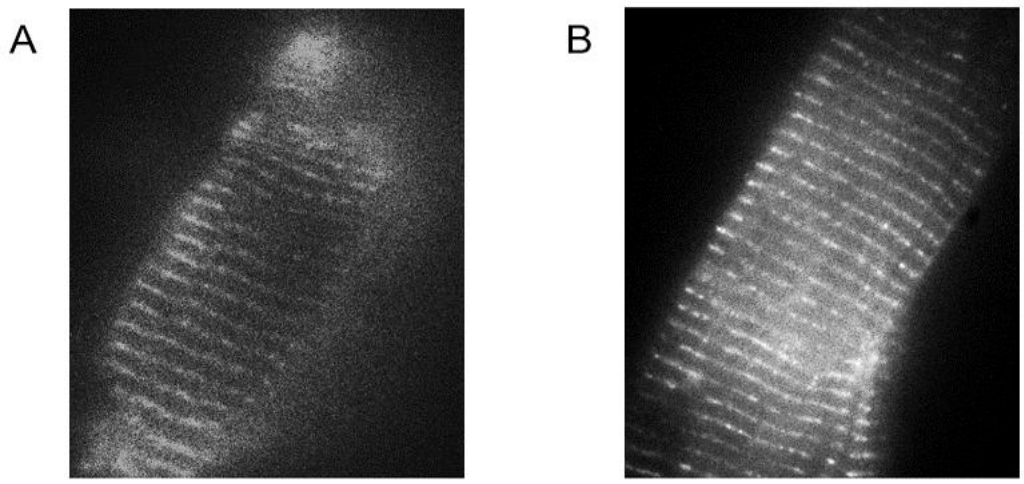

Figure 16. Fluorescent labelling of Z-discs in solution vs in flow chambers results in improved labelling. Samples A and B are both porcine cardiac LV myofibrils with 11 nM Monoclonal anti-α-actinin and 5.5 nM Alexa488 Goat anti-mouse IgG. **(A)** Incubation of myofibrils with fluorescent antibodies was carried out after the myofibrils were introduced into the imaging chamber. **(B)** Myofibril and antibody incubation was carried out in solution prior to the myofibrils being injected into the imaging chamber. Images were taken on the OAF microscope with the Orca Flash 4.2 camera and with the 488 nm diode Oxxius laser set to 18 mW.

Furthermore, to collect sufficient quantities of data, myofibrils need to have area large enough to accommodate high numbers of ATP binding events. To ensure myofibrils were large enough for this, the total homogenization time was reduced from 40 to 20 seconds. Subsequently, the average myofibril length was increased to ~27 µm (Figure 17).

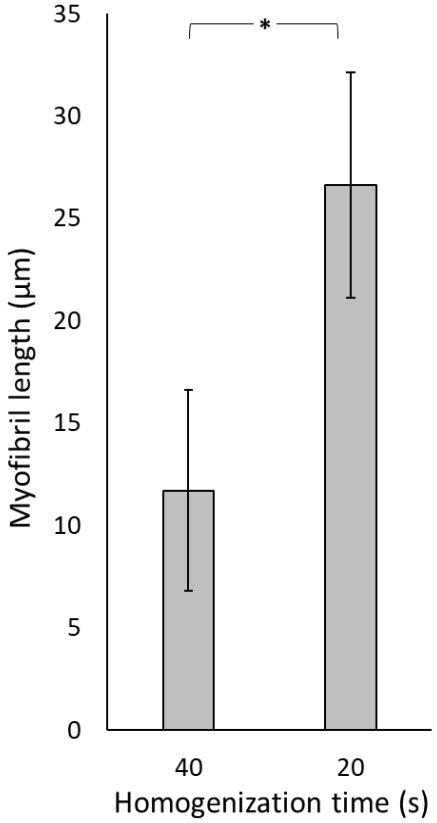

Figure 17. Decreasing homogenization time results in significant increase in myofibril length. To combat the short myofibrils, the tissue was homogenized for half the initial time used. The decrease from 40 seconds to 20 results in a significant and consistent increase in the length of myofibrils produced ($P < 0.5$). Errors bars are standard deviations. 40 seconds; 11.7 µm ($\pm$ 4.9 µm), n = 30 myofibrils. 20 seconds; 26.6 µm ($\pm$ 5.5 µm), n = 10 myofibrils. Statistical analysis performed was a two-tailed t-test, $P = 5 \times 10^{-6}$. * denotes $P < 0.05$.

Due to varied sizes of tissue from which myofibrils were isolated, the concentration of myofibrils in imaging chambers was inconsistent across preparations. These inconsistencies resulted in varied fluorescent antibody-to-myofibril ratios resulting in sample-to-sample variation of the fluorescent labelling quality. To address this, a strict criterion for which the OD_{600} of

the myofibril suspension had to fall within the range of 0.39 – 0.42 was introduced. With this, the concentration of myofibrils and their staining across sample preparations was more consistent than before.

3.2.2 Low Ionic Buffer Concentrations Resulted in Short Sarcomeres

Whole myofibril and individual sarcomere lengths were measured using the ImageJ plugin SarcOptiM (Pasqualin *et al.*, 2016) during the optimizations of myofibril preparations (Section 3.2.1). The average sarcomere length (SL) measured was ~24% shorter than the literature average (Figure 18; 1.44 µm $\pm$ 0.046 µm, n = 125 sarcomeres).

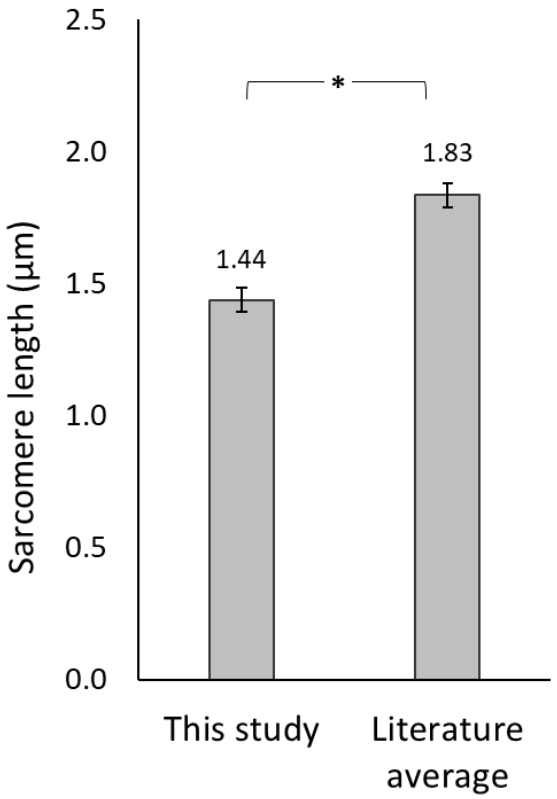

Figure 18. Cardiac sarcomeres are significantly shorted in this study than the literature average. Lengths of cardiac sarcomeres from this study (1.44 ± 0.05 µm) are compared to the literature average (1.83 ± 0.04 µm). A significant shortening of approximately 0.43 µm is observed in this study's myofibrils. Errors are standard deviations. Two-tailed t-test results in a P-value of 0.0017. * denotes $P < 0.05$.

To combat the short sarcomeres, small alterations were made to the existing protocol (Pilagov *et al.*, 2023). These included the addition of ATPase inhibitors, fluorescent labelling at room temperature (rather than 4 °C) and the removal of poly-l-lysine (PLL) from the imaging chamber (Belus *et al.*, 2008; Vikhorev, Ferenczi and Marston, 2016; Nelson *et al.*, 2023). None of these approaches resulted in a significant increase in sarcomere lengths (Figure 19; average SL of 1.5 µm ± 0.15 µm, n = 149 sarcomeres).

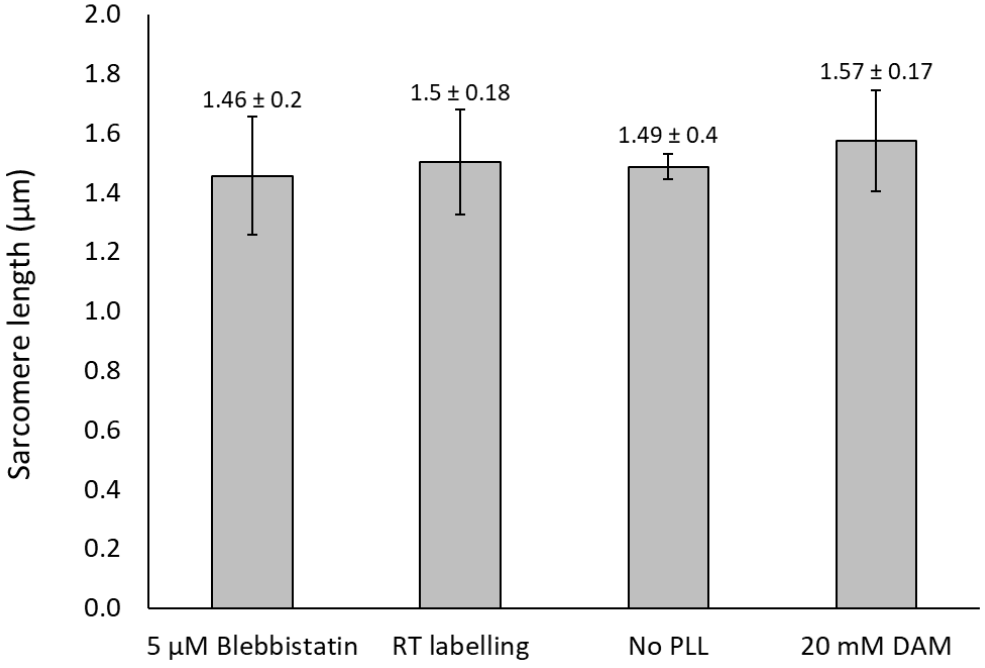

Figure 19. Effect of Experimental Modifications to Increase Porcine Cardiac Sarcomere Lengths. Comparison of the average sarcomere lengths from the experimental modifications; addition of 5 µM Blebbistatin, RT fluorescent labelling, no PLL in the imaging chamber and addition of 20 mM DAM. PLL = poly-l-lysine, DAM = diacetyl monoxime. Error bars are standard deviations. *Data collection supported in part by Matvey Pilagov and Sonette Steczina.*

Comparison of the preparation buffers used in the existing literature (Table 1) revealed that the buffers used for sample preparation had an ionic concentration 50 – 122 mM higher than what was being used in this study. This indicated the sarcomere shortening observed was potentially due to the low ionic strength (Brenner, Yu and Podolsky, 1984; Powers *et al.*, 2019). In

addition, it was also observed that freshly permeabilized tissue was used for myofibril isolation rather than tissue that had been permeabilized and then stored at -80 °C, as was done in this study.

Table 1. Comparison of ionic concentrations of sample preparation buffers

Study	Ionic concentration (mM)
Piroddi et al., 2006	200
Vikhorev et al., 2016	148
Nelson et al., 2023	129
This study	78

A comparison of sample preparation buffers revealed that the ionic concentration in preparation buffers used in this study is lower than that used across the literature.

The implementation of a high ionic concentration buffer, modified from (Vikhorev, Ferenczi and Marston, 2016) and the use of freshly permeabilized tissue, resulted in a significant increase in sarcomere lengths to those that are physiologically relevant and comparable to literature (Figure 20; 1.9 µm ± 0.09 µm, n = 98 sarcomeres). To ensure the length increase was a result of the higher ionic concentration, the previous buffer was flushed into the imaging chamber, this resulted in an immediate and significant length reduction (Figure 20; 1.35 µm ± 0.018 µm, n = 31 sarcomeres).

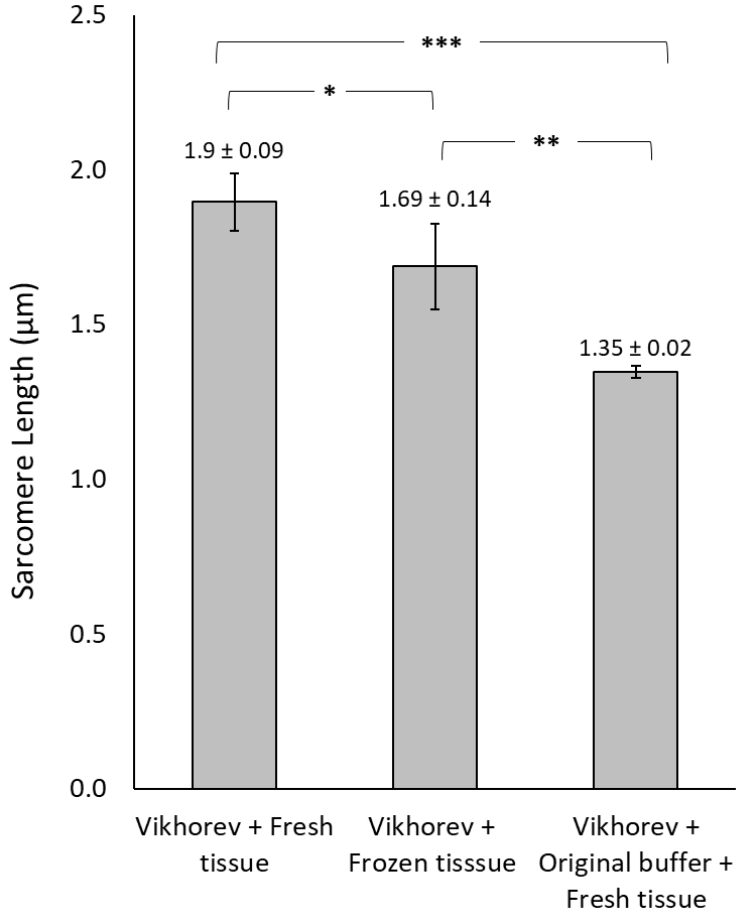

Figure 20. High ionic concentration results in physiologically relevant porcine cardiac sarcomere lengths. Comparison of the sarcomere lengths prepared with high ionic concentration buffer (modified from Vikhorev et al., 2016) with fresh and frozen permeabilized tissue and the original buffer flown in after incubation in the imaging chamber. Statistical analysis performed was a two-tailed t-test. * denotes P = 0.008, ** denotes P = 0.0003, *** denotes P = 0.000004. Errors are standard deviations. *Data collection supported in part by Matvey Pilagov and Sonette Steczina.*

Preliminary data confirming the effect of the high ionic concentration buffer was carried out with Tris in buffer solutions (Figure 20). However, replacing this with MOPS resulted in a more stable pH, therefore data collected from here onwards was done so with MOPS (Figure 21).

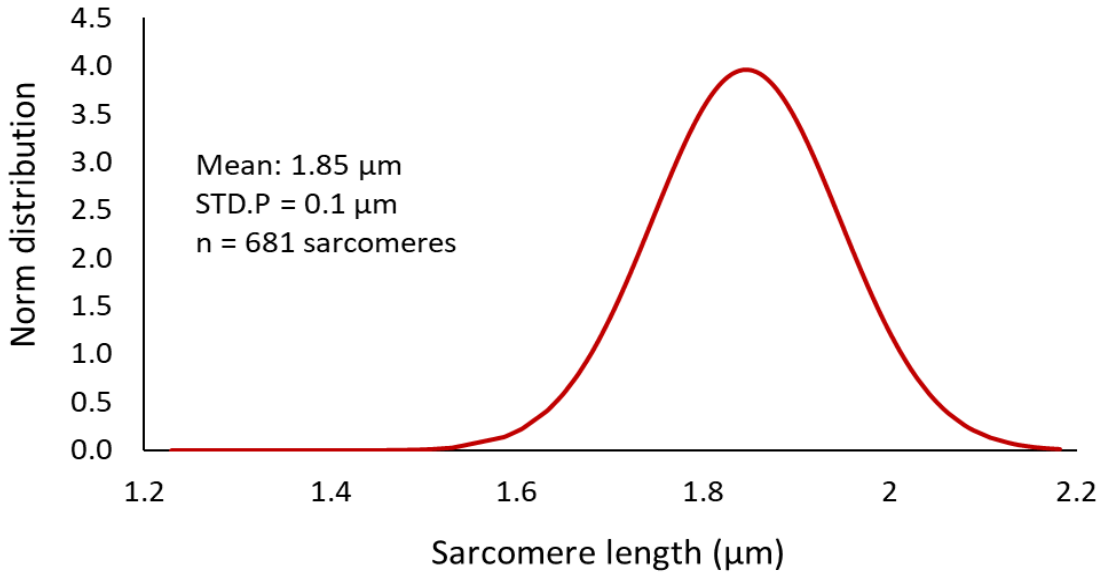

Figure 21. Sarcomere length distribution with optimized experimental conditions. Gaussian distribution of cardiac myofibril sarcomere lengths following all experimental optimizations. Optimized conditions include high ionic concentration buffer with MOPS (see section 2.1), tissue permeabilization on the day of data collection and addition of 20 mM BDM in sample preparations. Data presented is from three biological replicates. *Data collection supported in part by Matvey Pilagov and Sonette Steczina.*

3.2.3 Imaging the Binding of Single ATP Molecules in Cardiac Myofibrils Reveals Two Rates of ATP turnover.

The Cy3-ATP attachment durations were measured to determine the ATP turnover rates of individual myosins. These lifetimes were plotted as a cumulative residence time histogram (Figure 22) and best fit to three populations. The exponentials of these fits reveal rate constants of ~0.81 s^{-1}, ~0.098 s^{-1} and ~0.0064 s^{-1}, the first being consistent with non-specific binding (Amrute-Nayak *et al.*, 2014; Ušaj *et al.*, 2021), and the second and third being consistent with DRX and SRX myosin ATP turnover rates respectively (Hooijman, Stewart and Cooke, 2011; Nelson *et al.*, 2023; Pilagov *et al.*, 2023).

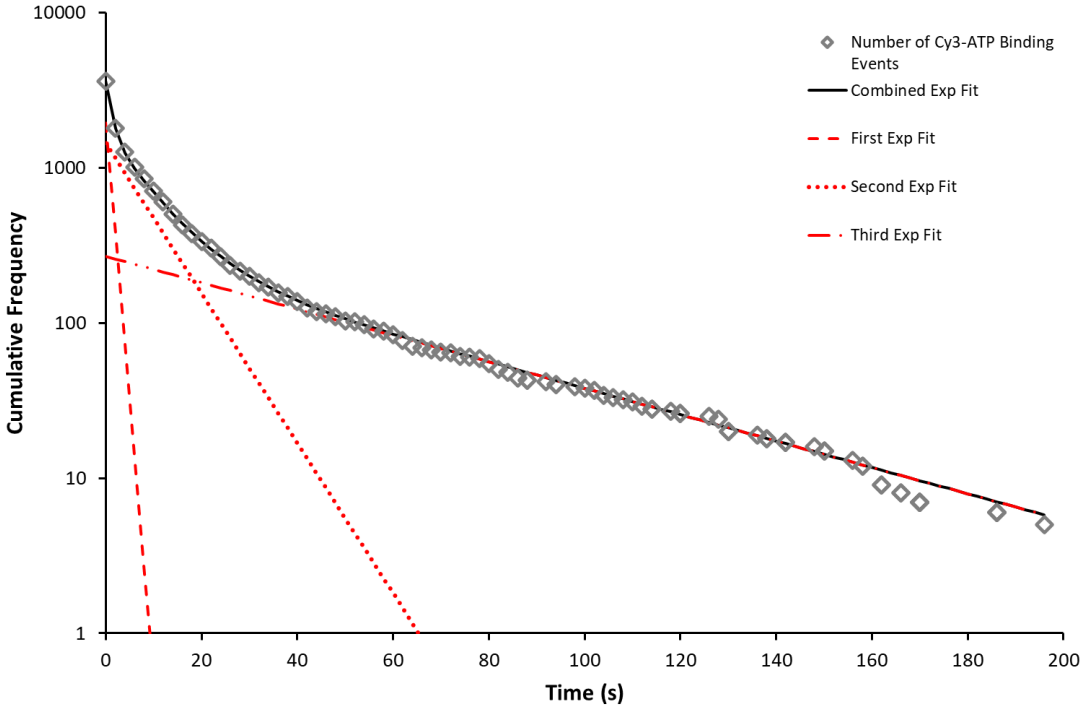

Figure 22. Cumulative residence time histogram showing all Cy3-ATP binding event durations. Lifetimes of all Cy3-ATP binding events were found to best fit to three exponentials (each shown in red) revealing the non-specific binding of Cy3-ATP (first exponential) and the two distinct rates of ATP turnover indicative of DRX and SRX myosin. Black line is the sum of all three exponentials. Y axis is on a logarithmic scale. N = 3 farm pigs, n = 3638 binding events. *Data collection supported in part by Matvey Pilagov and Sonette Steczina.*

4. Investigating the Spatial Distribution of SRX Myosin at High Resolution

4.1 Introduction

Determining the distribution of SRX myosin along the thick filament will provide data essential for understanding the regulatory processes of the sarcomere. The technique used for this study focused solely on the locations of binding events and not the event durations as was done in Chapter 3.

The ATP turnover rate of SRX myosin is slower than that of DRX myosin, therefore over the 30-minute imaging period, SRX myosin would turn over fewer Cy3-ATP molecules. Considering this, on cross-referencing the positions of binding events with the thick filament zones, regions with the lowest frequency of events would be indicative of those dominated by SRX myosin.

To observe only the initial location of the binding event and not the duration of the event, the Cy3-ATP molecule would have to become invisible to the camera while still being bound to myosin. Fortunately, fluorescent molecules undergo a phenomenon known as photobleaching in which the fluorophores lose their ability to fluoresce. The main pathway for photobleaching to occur is through photosensitized singlet oxygen reacting with the fluorophore's polymethine chain (Figure 10) causing it to break into smaller carbonyl products. Additional pathways include light-driven nucleophilic attacks on the polymethine chain resulting in reversible fluorescence decrease (Zheng and Lavis, 2017).

Under most circumstances, photobleaching is a limiting factor, for instance, when recording the ATP turnover rates (Chapter 3). Oxygen scavengers and

stroboscopic illumination (used in Chapter 3) slow the photobleaching of the molecule, preventing them from going dark prior to ATP turnover being completed. By utilizing photobleaching to the advantage of this novel technique, this phenomenon is no longer a limiting factor.

The strategy for determining which method was best suited to facilitate photobleaching is described in the following section of this chapter.

4.2 Results

Optimizations described from here onwards are in comparison to experimental conditions used for the investigation of myosin's ATP turnover rates (see Chapter 3).

4.2.1 Increasing Cy3-ATP Concentration for Increased Visible Binding Events Per Sample

Isolated cardiac myofibrils were to be fluorescently imaged with Cy3-ATP concentrations greater than that used in the investigation into the ATP cycling rates of myosin (see Chapter 3) to achieve a higher ratio of Cy3-ATP to ATP, therefore increasing the quantity of visible binding events per sample.

With raising the Cy3-ATP concentration approximately 7-fold, a significant ~28% shortening of the sarcomere lengths was observed (Figure 23; 1.32 µm ± 0.18 µm, n = 77 sarcomeres). A regeneration system of phosphoenolpyruvate (PEP) and pyruvate kinase (PK) was introduced to a Cy3-ATP stock prior to dilution in the final imaging buffer. At the same 7-fold concentration increase, the freshly regenerated Cy3-ATP showed to cause no significant decrease in sarcomere length ($P > 0.5$).

These results suggest the observed shortening of the sarcomeres were a result of ADP build-up, which was alleviated upon the introduction of the PK-PEP regeneration system. This system prevents ADP build-up by facilitating the continuous regeneration of ATP, whereby PK catalyses the transfer of the phosphate group from PEP (a high energy phosphate donor) to ADP, resulting in production of ATP (and pyruvate as a byproduct).

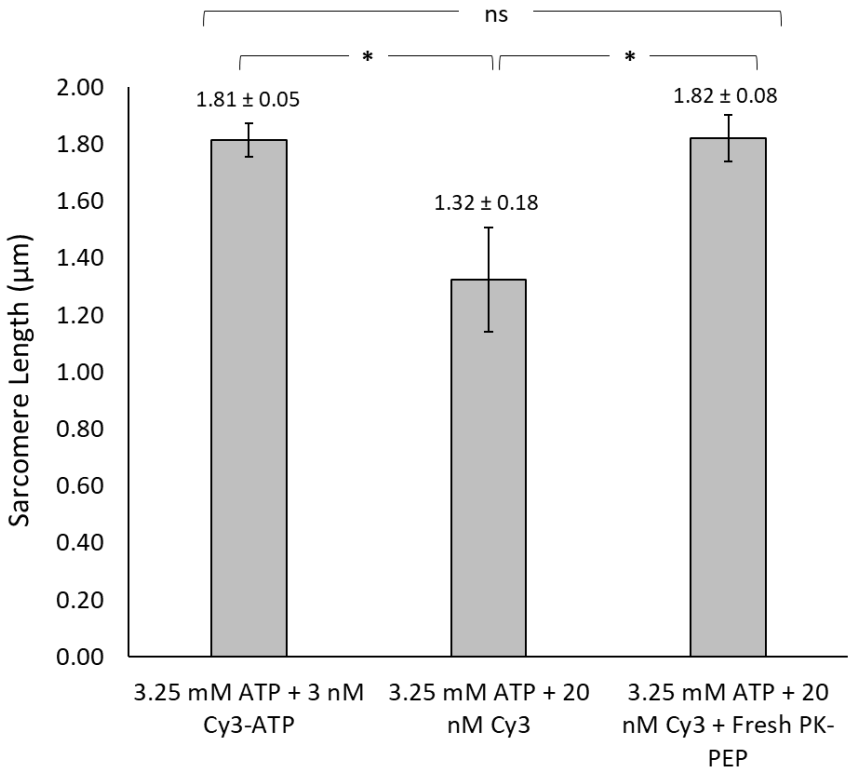

Figure 23. Impact of increasing Cy3-ATP concentration on sarcomere lengths. Comparison of sarcomere lengths following 7-fold increase of Cy3-ATP concentration pre- and post-addition of fresh PK-PEP regeneration system. Two tailed t-test showed that the sarcomere lengths collected with 20 nM Cy3-ATP without the fresh PK-PEP regeneration system were significantly shorter than those collected before the increase in Cy3-ATP concentration, or those collected with the 20 nM Cy3-ATP plus the PK-PEP, ($P = 0.00037$ and $P = 0.00024$ respectively). The addition of a fresh PK-PEP regeneration system was able to rectify the issue and sarcomere lengths were restored to an average length of 1.82 µm ($P > 0.05$). Errors are standard deviations. Statistical analysis performed was a two tailed t-test.

The increased Cy3-ATP concentration (20 nM) resulted in a Cy3-ATP/ATP binding events ratio of 1: ~163,000. Although an improvement from

the 1: ~1,000,000 when the Cy3-ATP concentration was at 3 nM, it was possible to further optimize this ratio by decreasing the ATP concentration. Reducing the concentration ~ 20-fold to 150 µM ATP (Warshaw *et al.*, 1990) resulted in a final Cy3-ATP/ATP binding events ratio of 1:7500 (20 nM Cy3-ATP: 150 µM ATP). These adjustments in concentration resulted in an average of 22 trackable events per 100 frames (n = 12), a ~ 75% increase compared to the 13 events per 100 frames (n = 9) observed under the previous imaging conditions (3 nM Cy3-ATP: 3.25 mM ATP).

4.2.2 Complete Photobleaching of Cy3-ATP Molecules Required Optimisations to the Imaging Approach

For the high-resolution mapping of binding events, photobleaching of the fluorescent Cy3-ATP molecules after the acquisition of each frame was necessary (Figure 24). This was achieved by increasing the intensity of the 561 nm laser to 40 mW and keeping the laser on continuously rather than utilizing stroboscopic illumination. Furthermore, the time between each frame was increased to 5 seconds, allowing more time in between frame acquisition to ensure that all fluorescent molecules imaged in the previous frame were photobleached. Oxygen scavengers (Trolox), used for preservation of fluorescence in Chapter 3, were omitted from the imaging buffer.

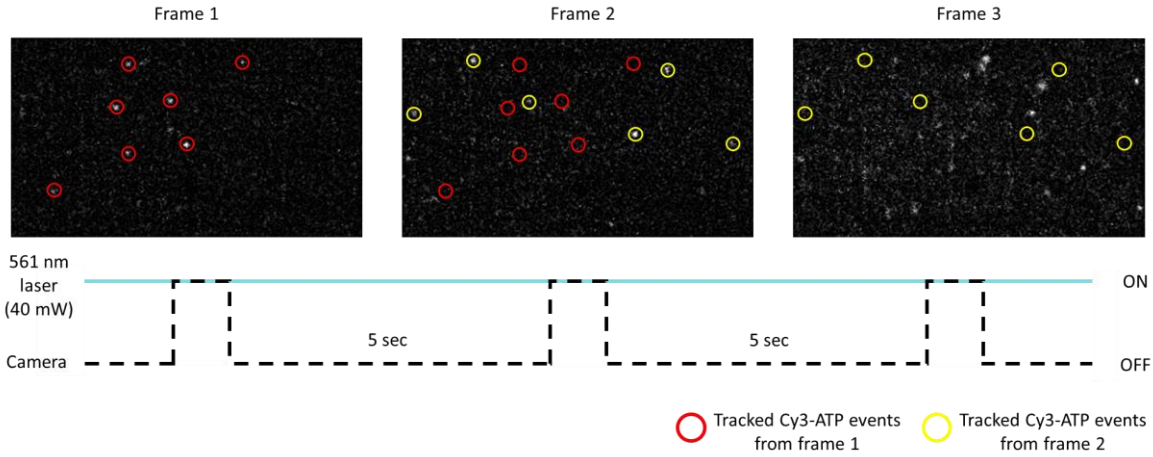

Figure 24. Continuous illumination and increased laser power ensures complete photobleach of imaged Cy3-ATP binding events. Red circles show the positions of events tracked from frame 1, these same tracks are displayed on frame 2, showing that no events appear in the same position and therefore complete photobleaching was achieved. This is also shown for tracked events in frame 2 not being imaged in frame 3 (yellow circles). Image contrast was increased here for ease of viewing.

4.2.3 High-Resolution Spatial Distribution of SRX Myosin

Cy3-ATP binding event positions extracted using Trackmate (Figure 14), were binned into sarcomere zones (Figure 25A). The central M-line position was determined by the midpoint between each sarcomere's Z-discs. The coordinates for the zone boundaries were determined by relating zone sizes to the central M-line. The P-zone, 80-160 nm from the M-line contains 18 myosin crowns. The C-zone is the largest, spanning from the P-zone to 500 nm away from the M-line. This zone is comprised of 26 myosin crowns and contains the cMyBP-C. The D-zone expands from the C-zone to ~800 nm from the M line and contains 5 myosin crowns. Finally, the bare zone, is the region closest to M-line and neighbours the P-zone and is absent of myosin crowns and cMyBP-C (Tonino *et al.*, 2019; Tamborrini *et al.*, 2023).

With zonal boundaries calculated, the x coordinates for each tracked binding event were binned into their respective sarcomeric zones and this is presented as the number of observed binding events per myosin crown in each zone. Doing so revealed a drop in activity in the C-zone in comparison to the neighbouring zones (Figure 25A). This high-resolution imaging approach resulted in the ability for highly specific localization of binding events within the sarcomere zone, with a positional accuracy of ~ 30 nm (Pilagov et al., 2023). Therefore, it was possible to localize the binding events to 30 nm regions (Figure 25B). This high-resolution map revealed a spike in activity at the borders of the sub-sarcomere zones.

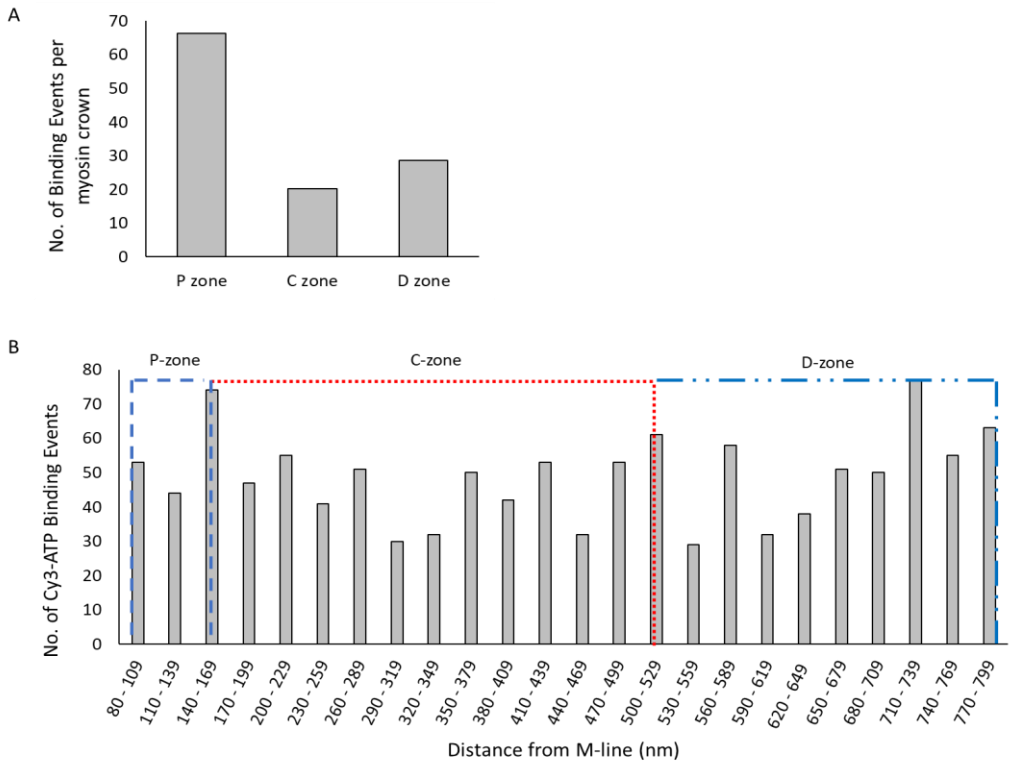

Figure 25. Spatial Distribution of Observed ATP-Binding Events Across the Thick Filament. A) Myosin ATP turnover activity as represented by the number of Cy3-ATP binding events per myosin crown per sarcomere zone. Sarcomere zones are not equal in size and so do not contain the same amount of myosin crowns. Therefore, to describe the relative activity levels within each zone, the data are presented as the number of Cy3-ATP binding events per myosin crown rather than a total number of events per zone. **B)** Mapping of Cy3-ATP binding across the thick filament A-band. Binding event frequencies are binned at 30 nm. P- C- and D- zones are highlighted, N = 3 pigs, 149 sarcomeres, n = 1099 tracked events. For data processing see Figure 14.

5. Discussion

Cardiac contractility is tightly regulated through finely tuned interactions between the thick and thin filaments of the sarcomere. These regulatory processes primarily influence the binding affinity of the motor protein, myosin with actin of the thin filament. This binding is regulated by the blocking of binding sites on actin by accessory proteins, troponin and tropomyosin in the absence of calcium. The mechanisms behind how these regulatory proteins function is well-researched and understood (Yamada, Namba and Fujii, 2020). On the other hand, regulation of the thick filament occurs through myosin populations that adopt distinct biochemical states influencing their rates of ATP turnover; the disordered relaxed (DRX) and super relaxed (SRX) states. The DRX population of myosin exhibit an ATP turnover rate of ~ 0.03 s^{-1} whereas for the SRX population, this is up to 10-fold slower (Hooijman, Stewart and Cooke, 2011; Nelson *et al.*, 2023; Pilagov *et al.*, 2023). Specifically in cardiac muscle, both populations exist in the presence and absence of calcium activation, potentiating a cardioprotective mechanism to preserve energy. However, the regulation and spatial distribution of these myosin populations across the thick filament is yet to be fully understood. Furthermore, there are currently no measurements of these rates in β-HCM cardiac myofibrils, the dominant isoform in human left ventricular cardiac tissue, and the isoform in which ~40% of HCM-causing mutations occur.

The aim of this thesis was the optimization of the single molecule tracking of Cy3-ATP in cardiac tissue to enable the measurement of DRX and SRX myosin populations and ATP hydrolysis rates in porcine cardiac left ventricular tissue. Previous studies have reported rates for cardiac tissue

however this is the first study in which spatiotemporal measurements were carried out in β-MHC cardiac tissue. We also aimed to develop a novel high-resolution imaging technique to facilitate the precise localization of SRX myosin-dominated regions across the thick filament. With this, we also open the possibility of uncovering any cooperativity at the interface of sub-sarcomeric zones.

The major findings of this study are the two distinct ATP turnover rates measured in porcine cardiac left ventricular tissue which align with the reported DRX and SRX rates, confirming the validity of this imaging technique. We also were able to successfully develop a novel imaging technique to facilitate spatial mapping of myosin activity across the thick filament at a spatial resolution of ~30 nm.

5.1 Two Biochemically Distinct Relaxed Myosin Populations

The single-molecule tracking of Cy3-ATP binding event lifetimes in porcine cardiac left ventricle myofibrils revealed ATP turnover rates that align with those expected for DRX and SRX myosin (Figure 22). We report a DRX lifetime of 10.2 - 30 s and ~156.3 s for SRX, this approximately 10-fold increase in SRX lifetime is consistent with previously reported rates measured for skeletal and cardiac myosin (Figure 11) (Nelson *et al.*, 2020, 2023; Walklate *et al.*, 2022; Pilagov *et al.*, 2023). These results and their consistency with the literature provide evidence that this imaging technique and optimised experimental conditions are a robust and reliable approach for the measurement of myosin ATP turnover kinetics in cardiac myofibrils.

5.2 High-resolution spatial mapping reveals potential crosstalk at the interface of sub-sarcomere zones

The regulatory protein, cardiac myosin binding protein-C (cMyBP-C), localised to the thick filament C-zone, is shown to sequester myosin into the SRX state (McNamara, Singh and Sadayappan, 2019; Heling, Geeves and Kad, 2020; Nelson *et al.*, 2023) . This suggests that SRX myosin density is expected to peak in the cMyBP-C containing C-zone region, hence the potential for the spatially defined regions of the filament having unique regulation and ATP consumption. Furthermore, neighbouring myosins at the interface between sub-sarcomeric zones may exhibit cooperative interactions, suggesting the possibility of 'crosstalk'.

High-resolution, spatial mapping of ATP consumption across the porcine cardiac β-myosin dominated thick filament highlights a clear reduction in activity in the C-zone region (Figure 25A). This reduction in activity indicates slower ATP turnover throughout the whole zone, hence a larger population of SRX myosin in comparison to the P- and D-zones. This finding is consistent with reports of the C-zone localized cMyBP-C sequestering these myosins into the SRX state (McNamara *et al.*, 2016; McNamara, Singh and Sadayappan, 2019; Huang *et al.*, 2023; Nelson *et al.*, 2023).

Closer examination of the ATP consumption reveals a spike in activity at the zonal borders between the P- and C-zones and the C- and D-zones (Figure 25B). This may be an indicator of cooperativity between myosins at the interface between the sub-sarcomeric zones.

However, it is important to note that the data presented here allows for confirmation of the validity of this technique but, any conclusions made are

preliminary and a higher n (Figure 25) is required to fully understand this potential cooperativity.

6. Conclusions and Future Work

The successful development of a high-resolution, spatial mapping imaging technique designed to determine the distribution of myosins in the SRX state along the thick filament at a nm level, has opened the possibility of developing a much more nuanced understanding of thick filament regulation. This imaging technique makes it possible, for the first time, to visualise potential crosstalk at the borders of sub-sarcomere zones through monitoring ATP turnover. Utilization of this technique to image myosin activity in cMyBP-C knockout mice cardiac myofibrils (Harris *et al.*, 2002) would provide further understanding of the role cMyBP-C plays in thick filament regulation. In addition, by labelling phosphorylated versus non-phosphorylated cMyBP-C we might even be able to observe the precise effects on nearby myosin activity.

As this technique is still evolving, continued refinement is essential to improve its performance. Such improvements include finetuning laser power and exposure time to maximise the SNR and stabilizing samples in imaging chambers to mitigate myofibril drift. To achieve higher spatial resolution such as that used to localise fluorophore centroids in Fluorescence Imaging with One-Nanometre Accuracy (FIONA) will require precise computational analysis (Wang *et al.*, 2014). Adopting such improvements and adapting methodologies from establish high-resolution imaging techniques could enable spatial resolution at the level of individual myosin crowns (43 nm separation). By firstly optimizing this combined approach using untreated

porcine cardiac myofibrils will enable this technique to be employed to investigate ATP turnover in a variety of samples; for example, samples with HCM-causing mutations and those treated with drugs such as Mavacamten, a cardiac myosin inhibitor used for the treatment of HCM (Kawas *et al.*, 2017).

To conclude, the work presented in this thesis provides the foundation for a multitude of studies to contribute to the complete understanding of thick filament regulation in cardiac myofibrils.

7. Bibliography

Adhikari, A.S. *et al.* (2019) 'β-Cardiac myosin hypertrophic cardiomyopathy mutations release sequestered heads and increase enzymatic activity', *Nature Communications*, 10(1), p. 2685. Available at: https://doi.org/10.1038/s41467-019-10555-9.

Amrute-Nayak, M. *et al.* (2014) 'ATP turnover by individual myosin molecules hints at two conformers of the myosin active site', *Proceedings of the National Academy of Sciences*, 111(7), pp. 2536–2541. Available at: https://doi.org/10.1073/pnas.1316390111.

Belus, A. *et al.* (2008) 'The familial hypertrophic cardiomyopathy-associated myosin mutation R403Q accelerates tension generation and relaxation of human cardiac myofibrils', *The Journal of Physiology*, 586(15), pp. 3639–3644. Available at: https://doi.org/10.1113/jphysiol.2008.155952.

Blair, E. *et al.* (2002) 'Mutations of the Light Meromyosin Domain of the β-Myosin Heavy Chain Rod in Hypertrophic Cardiomyopathy', *Circulation Research*, 90(3), pp. 263–269. Available at: https://doi.org/10.1161/hh0302.104532.

Brant B. Hafen and Bracken Burns (2018) *Physiology, Smooth Muscle*, *StatPearls, StatPearls Publishing*. Available at: https://www.ncbi.nlm.nih.gov/books/NBK526125/ (Accessed: 15 September 2023).

Brenner, B., Yu, L.C. and Podolsky, R.J. (1984) *X-RAY DIFFRACTION EVIDENCE FOR CROSS-BRIDGE FORMATION IN RELAXED MUSCLE FIBERS AT VARIOUS IONIC STRENGTHS*.

Desai, R., Geeves, M.A. and Kad, N.M. (2015) 'Using Fluorescent Myosin to Directly Visualize Cooperative Activation of Thin Filaments', *The Journal of Biological Chemistry*, 290(4), p. 1915. Available at: https://doi.org/10.1074/JBC.M114.609743.

Fish, K.N. (2022) 'Total Internal Reflection Fluorescence (TIRF) Microscopy', *Current Protocols*, 2(8), p. e517. Available at: https://doi.org/10.1002/CPZ1.517.

Fordham, M., Amos, W.B. and White, J.G. (1987) 'Use of confocal imaging in the study of biological structures', *Applied Optics, Vol. 26, Issue 16, pp. 3239-3243*, 26(16), pp. 3239–3243. Available at: https://doi.org/10.1364/AO.26.003239.

Frontera, W.R. and Ochala, J. (2015) 'Skeletal Muscle: A Brief Review of Structure and Function', *Calcified Tissue International*, 96(3), pp. 183–195. Available at: https://doi.org/10.1007/s00223-014-9915-y.

Hanson, J. and Huxley, H.E. (1953) 'Structural Basis of the Cross-Striations in Muscle', *Nature*, 172(4377), pp. 530–532. Available at: https://doi.org/10.1038/172530b0.

Harris, S.P. *et al.* (2002) 'Hypertrophic cardiomyopathy in cardiac myosin binding protein-C knockout mice', *Circulation Research*, 90(5), pp. 594–601. Available at: https://doi.org/10.1161/01.RES.0000012222.70819.64/SUPPL_FILE/3689-R1_ONLINE.PDF.

Heeransh D. Dave, Micah Shook and Matthew Varacallo (2018) *Anatomy, Skeletal Muscle*, *StatPearls, StatPearls Publishing*. Available at: https://www.ncbi.nlm.nih.gov/books/NBK537236/ (Accessed: 15 September 2023).

Heissler, S.M. *et al.* (2021) 'Cryo-EM structure of the autoinhibited state of myosin-2', *Science Advances*, 7(52). Available at: https://doi.org/10.1126/sciadv.abk3273.

Heling, L.W.H.J., Geeves, M.A. and Kad, N.M. (2020) 'MyBP-C: one protein to govern them all', *Journal of Muscle Research and Cell Motility*, 41(1), pp. 91–101. Available at: https://doi.org/10.1007/s10974-019-09567-1.

Hooijman, P., Stewart, M.A. and Cooke, R. (2011) 'A New State of Cardiac Myosin with Very Slow ATP Turnover: A Potential Cardioprotective Mechanism in the Heart', *Biophysical Journal*, 100(8), pp. 1969–1976. Available at: https://doi.org/10.1016/j.bpj.2011.02.061.

Huang, X. *et al.* (2023) 'Cryo-electron tomography of intact cardiac muscle reveals myosin binding protein-C linking myosin and actin filaments', *Journal of Muscle Research and Cell Motility* [Preprint]. Available at: https://doi.org/10.1007/s10974-023-09647-3.

Huxley, A.F. (1957) 'Muscle structure and theories of contraction.', *Progress in biophysics and biophysical chemistry*, 7, pp. 255–318.

Huxley, A.F. and Niedergerke, R. (1954) 'Structural Changes in Muscle During Contraction: Interference Microscopy of Living Muscle Fibres', *Nature*, 173(4412), pp. 971–973. Available at: https://doi.org/10.1038/173971a0.

Kampourakis, T., Sun, Y.-B. and Irving, M. (2016) 'Myosin light chain phosphorylation enhances contraction of heart muscle via structural changes in both thick and thin filaments', *Proceedings of the National Academy of Sciences*, 113(21). Available at: https://doi.org/10.1073/pnas.1602776113.

Kawas, R.F. *et al.* (2017) 'A small-molecule modulator of cardiac myosin acts on multiple stages of the myosin chemomechanical cycle', *Journal of Biological Chemistry*, 292(40), pp. 16571–16577. Available at: https://doi.org/10.1074/jbc.M117.776815.

Kensler, R.W. and Harris, S.P. (2008) 'The Structure of Isolated Cardiac Myosin Thick Filaments from Cardiac Myosin Binding Protein-C Knockout Mice', *Biophysical Journal*, 94(5), pp. 1707–1718. Available at: https://doi.org/10.1529/biophysj.107.115899.

Lamber, E.P., Guicheney, P. and Pinotsis, N. (2022) 'The role of the M-band myomesin proteins in muscle integrity and cardiac disease', *Journal of Biomedical Science*, 29(1), p. 18. Available at: https://doi.org/10.1186/s12929-022-00801-6.

Laurens Heling (2019) *Biochemical Mapping of Myofibrillar ATPase using STORM Imaging*. University of Kent.

Liu, X. *et al.* (2016) 'Mammalian Nonmuscle Myosin II Binds to Anionic Phospholipids with Concomitant Dissociation of the Regulatory Light Chain', *Journal of Biological Chemistry*, 291(48), pp. 24828–24837. Available at: https://doi.org/10.1074/jbc.M116.739185.

McNamara, J.W. *et al.* (2016) 'Ablation of cardiac myosin binding protein-C disrupts the super-relaxed state of myosin in murine cardiomyocytes', *Journal of Molecular and Cellular Cardiology*, 94, pp. 65–71. Available at: https://doi.org/10.1016/j.yjmcc.2016.03.009.

McNamara, J.W., Singh, R.R. and Sadayappan, S. (2019) 'Cardiac myosin binding protein-C phosphorylation regulates the super-relaxed state of myosin', *Proceedings of the National Academy of Sciences of the United States of America*, 116(24), pp. 11731–11736. Available at: https://doi.org/10.1073/PNAS.1821660116/SUPPL_FILE/PNAS.1821660116.SAPP.PDF.

Miller, M.S. *et al.* (2009) 'Alternative S2 hinge regions of the myosin rod affect myofibrillar structure and myosin kinetics', *Biophysical Journal*, 96(10), pp. 4132–4143. Available at: https://doi.org/10.1016/J.BPJ.2009.02.034/ASSET/348C7C10-C0EF-407A-970F-070B0F4B6228/MAIN.ASSETS/GR5.JPG.

mpicbg-scicomp (2017) *Manual Drift Correction Plugin*, *GitHub*. Available at: https://github.com/mpicbg-scicomp/Manual_drift_correction (Accessed: 26 November 2024).

Myburgh, K.H., Franks-Skiba, K. and Cooke, R. (1995) 'Nucleotide turnover rate measured in fully relaxed rabbit skeletal muscle myofibrils.', *The Journal of general physiology*, 106(5), pp. 957–973. Available at: https://doi.org/10.1085/jgp.106.5.957.

Nelson, S. *et al.* (2023) 'Myosin-binding protein C stabilizes, but is not the sole determinant of SRX myosin in cardiac muscle', *Journal of General Physiology*, 155(4). Available at: https://doi.org/10.1085/jgp.202213276.

Nelson, S.R. *et al.* (2020) 'Imaging ATP Consumption in Resting Skeletal Muscle: One Molecule at a Time', *Biophysical Journal*, 119(6), pp. 1050–1055. Available at: https://doi.org/10.1016/j.bpj.2020.07.036.

Pasqualin, C. *et al.* (2016) 'SarcOptiM for ImageJ: high-frequency online sarcomere length computing on stimulated cardiomyocytes', *American journal of physiology. Cell physiology*, 311(2), pp. C277–C283. Available at: https://doi.org/10.1152/AJPCELL.00094.2016.

Pilagov, M. *et al.* (2023) 'Single-molecule imaging reveals how mavacamten and PKA modulate ATP turnover in skeletal muscle myofibrils'. Available at: https://doi.org/10.1085/jgp.202213087.

Powers, J.D. *et al.* (2019) 'Cardiac myosin activation with 2-deoxy-ATP via increased electrostatic interactions with actin', *Proceedings of the National Academy of Sciences of the United States of America*, 166(23), pp. 11502–11507. Available at: https://doi.org/10.1073/pnas.1905028116.

Rashelle Ripa *et al.* (2023) *Physiology, Cardiac Muscle*, *StatPearls, StatPearls Publishing*. Available at: https://www.ncbi.nlm.nih.gov/books/NBK572070 (Accessed: 15 September 2023).

Vander Roest, A.S. *et al.* (2021) 'Hypertrophic cardiomyopathy β-cardiac myosin mutation (P710R) leads to hypercontractility by disrupting super relaxed state', *Proceedings of the National Academy of Sciences*, 118(24). Available at: https://doi.org/10.1073/pnas.2025030118.

Schindelin, J. *et al.* (2012) 'Fiji - an Open Source platform for biological image analysis', *Nature methods*, 9(7), pp. 676–682. Available at: https://doi.org/10.1038/NMETH.2019.

Schmid, M. and Toepfer, C.N. (2021) 'Cardiac myosin super relaxation (SRX): a perspective on fundamental biology, human disease and therapeutics', *Biology Open*, 10(2). Available at: https://doi.org/10.1242/bio.057646.

Stelzer, J.E., Fitzsimons, D.P. and Moss, R.L. (2006) 'Ablation of Myosin-Binding Protein-C Accelerates Force Development in Mouse Myocardium', *Biophysical Journal*, 90(11), pp. 4119–4127. Available at: https://doi.org/10.1529/biophysj.105.078147.

Stewart, M.A. *et al.* (2010) 'Myosin ATP turnover rate is a mechanism involved in thermogenesis in resting skeletal muscle fibers', *Proceedings of the National Academy of Sciences*, 107(1), pp. 430–435. Available at: https://doi.org/10.1073/pnas.0909468107.

Suggs, J.A. *et al.* (2007) 'Alternative S2 Hinge Regions of the Myosin Rod Differentially Affect Muscle Function, Myofibril Dimensions and Myosin Tail Length', *Journal of Molecular Biology*, 367(5), pp. 1312–1329. Available at: https://doi.org/10.1016/J.JMB.2007.01.045.

Tamborrini, D. *et al.* (2023) 'Structure of the native myosin filament in the relaxed cardiac sarcomere', *Nature*, 623(7988), p. 863. Available at: https://doi.org/10.1038/S41586-023-06690-5.

Tinevez, J.Y. *et al.* (2017) 'TrackMate: An open and extensible platform for single-particle tracking', *Methods*, 115, pp. 80–90. Available at: https://doi.org/10.1016/J.YMETH.2016.09.016.

Toepfer, C.N. *et al.* (2020) 'Myosin Sequestration Regulates Sarcomere Function, Cardiomyocyte Energetics, and Metabolism, Informing the Pathogenesis of Hypertrophic Cardiomyopathy', *Circulation*, 141(10), pp. 828–842. Available at: https://doi.org/10.1161/CIRCULATIONAHA.119.042339/SUPPL_FILE/CIRC_CIRCULATIONAHA-2019-042339_SUPP1.PDF.

Tonino, P. *et al.* (2017) 'The giant protein titin regulates the length of the striated muscle thick filament', *Nature Communications*, 8(1), p. 1041. Available at: https://doi.org/10.1038/s41467-017-01144-9.

Tonino, P. *et al.* (2019) 'Fine mapping titin's C-zone: Matching cardiac myosin-binding protein C stripes with titin's super-repeats'. Available at: https://doi.org/10.1016/j.yjmcc.2019.05.026.

Toseland, C.P. and Webb, M.R. (2011) 'Fluorescent nucleoside triphosphates for single-molecule enzymology', *Methods in Molecular Biology*, 778, pp. 161–174. Available at: https://doi.org/10.1007/978-1-61779-261-8_11/FIGURES/2_11.

Towbin, J.A. (2009) 'Hypertrophic Cardiomyopathy', *Pacing and Clinical Electrophysiology*, 32(s2), pp. S23–S31. Available at: https://doi.org/10.1111/j.1540-8159.2009.02381.x.

Ušaj, M. *et al.* (2021) 'Single molecule turnover of fluorescent ATP by myosin and actomyosin unveil elusive enzymatic mechanisms', *Communications Biology*, 4(1). Available at: https://doi.org/10.1038/s42003-020-01574-0.

Vikhorev, P.G., Ferenczi, M.A. and Marston, S.B. (2016) 'Instrumentation to study myofibril mechanics from static to artificial simulations of cardiac cycle'. Available at: https://doi.org/10.1016/j.mex.2016.02.006.

Walklate, J. *et al.* (2022) 'Exploring the super-relaxed state of myosin in myofibrils from fast-twitch, slow-twitch, and cardiac muscle', *The Journal of Biological Chemistry*, 298(3), p. 101640. Available at: https://doi.org/10.1016/J.JBC.2022.101640.

Wang, Y. *et al.* (2014) 'Fluorescence Imaging with One-nanometer Accuracy (FIONA)', *Journal of Visualized Experiments (JoVE)*, (91), p. e51774. Available at: https://doi.org/10.3791/51774.

Wang, Z. *et al.* (2021) 'The molecular basis for sarcomere organization in vertebrate skeletal muscle', *Cell*, 184(8), p. 2135. Available at: https://doi.org/10.1016/J.CELL.2021.02.047.

Warshaw, D.M. *et al.* (1990) *Smooth Muscle Myosin Cross-bridge Interactions Modulate Actin Filament Sliding Velocity In Vitro*. Available at: www.jcb.org.

Webb, D.J. and Brown, C.M. (2012) 'Epi-Fluorescence Microscopy', pp. 29–59. Available at: https://doi.org/10.1007/978-1-62703-056-4_2.

Woo, A. *et al.* (2003) 'Mutations of the myosin heavy chain gene in hypertrophic cardiomyopathy: critical functional sites determine prognosis', *Heart*, 89(10), pp. 1179–1185. Available at: https://doi.org/10.1136/heart.89.10.1179.

Yamada, Y., Namba, K. and Fujii, T. (2020) 'Cardiac muscle thin filament structures reveal calcium regulatory mechanism', *Nature Communications*, 11(1), p. 153. Available at: https://doi.org/10.1038/s41467-019-14008-1.

Zheng, Q. and Lavis, L.D. (2017) 'Development of photostable fluorophores for molecular imaging', *Current Opinion in Chemical Biology*, 39, pp. 32–38. Available at: https://doi.org/10.1016/J.CBPA.2017.04.017.

Zoghbi, M.E. *et al.* (2008) 'Three-dimensional structure of vertebrate cardiac muscle myosin filaments', *Proceedings of the National Academy of Sciences*, 105(7), pp. 2386–2390. Available at: https://doi.org/10.1073/pnas.0708912105.